TRAJECTORY ANALYSIS AND DESIGN FOR PLANETARY POWERED DESCENT AND ORBITAL ASCENT MANEUVERS

A THESIS SUBMITTED TO THE GRADUATE DIVISION OF THE UNIVERSITY OF HAWAIʻI AT MĀNOA IN PARTIAL FULFUILLMENT OF THE REQUIREMENTS FOR THE DEGREE OF

MASTER OF SCIENCE

IN

MECHANICAL ENGINEERING

FALL 2019

By

Melissa M. Onishi

Thesis Committee:

Dilmurat Azimov, Chairperson
John Allen
Sarah Post
Trevor Sorensen

ABSTRACT

NASA's past Mars missions such as Mars Pathfinder, the Mars Exploration Rovers and the Mars Science Laboratory projects have led to the necessity of designing the next generation of landers, one of the goals of which is to achieve safe, velocity of less than 1 m/s and precise landing, within 100 m from the designated landing site. Previous studies focused on the formulation of manifolds of initial and final points for atmospheric entry, powered descent and landing. These manifolds can be generated by a construction of envelopes of the maneuver trajectories using a vast range of terminal conditions for the trajectory and lander's parameters. This paper describes the design, analysis and construction of trajectory envelopes for accurate landing maneuvers. A family of envelopes is generated by varying a vast range of terminal conditions to satisfy the proposed design space based on previous Mars missions. The following phases are considered in the landing maneuvers: exoatmospheric thrust phase, atmospheric transit phase and powered descent and landing phase. The entry velocity components were compared in two cases where the velocity component in the y-direction, v_{y0} is zero or a nonzero constant with several fixed conditions to analyze the overall profile of the entry trajectory. From case B, where v_{y0} is a nonzero constant, one of the trajectories achieved a landing altitude of 0.3891 m, velocity of 0.0015 m/s and distance of 88. 02559 m from the designated landing site. Specific parameters are designated to satisfy the proposed design space and achieve accurate landing. The continuity conditions at the junction points have been presented and analyzed to provide smooth and continuous change of these parameters except for the control variables. The proposed design and construction of trajectory envelopes can be used in the mission design analysis for landing missions. This study also proposes rudimentary solutions for lunar descent and ascent maneuvers in anticipation for sample return missions on the Moon.

Table of Contents

LIST OF TABLES

LIST OF FIGURES

NONMENCLATURE

A	frontal area of the spacecraft, (m^2)
BA	atmospheric transit phase
BP	backward propagation
c	exhaust velocity, (m/s)
C_D	drag coefficient
$\cos\alpha, \cos\beta, \cos\gamma$	thrust direction cosine in the x, y, z direction, (º)
D	atmospheric drag, (N)
D_x, D_y, D_z	atmospheric drag in the x, y, z direction, (N)
e	eccentricity
EDL	entry, descent and landing
FP	forward propagation
g_0	gravity on Earth, (m/s^2)
g_M	gravity on Mars, (m/s^2)
g_m	gravity on Moon, (m/s^2)
h	altitude, (m)
Isp	specific impulse, (s)
L	landing phase
LA	lunar ascent
LD	lunar descent
LS	landing site
m	mass of the lander, (kg)
m_0	initial mass, (kg)
$\dot{m}$	mass flow rate, (kg/s)
p	semi latus rectum, (m)
r	radial distance, (m)
Req_M	Mars equatorial radius, (m)

Req_m	Moon equatorial radius, (m)
TA1	exoatmospheric thrust phase
TA2	powered descent phase
t	time, (s)
t_i	initial time, (s)
t_f	final time, (s)
T/W	thrust-to-weight ratio
u	argument of latitude at epoch, (º)
v	magnitude of velocity vector, (m/s)
v_r	radial velocity component, (m/s)
v_f	velocity normal to position vector, (m/s)
v_{rel}	relative velocity, (m/s)
v_x, v_y, v_z	velocity vector in the *x*, *y*, *z* direction, (m/s)
x_{LS}, y_{LS}, z_{LS}	*x*, *y*, *z* component for landing site, (m)
$\Delta\varepsilon_\alpha$, $\Delta\varepsilon_\beta$, $\Delta\varepsilon_\gamma$	error of thrust direction angle in the *x*, *y*, *z* direction, (º)
γ	flight path angle, (º)
η	thrust-vector angle, (º)
ϕ	azimuthal angle for a spherical coordinate system, (º)
ϕ_{LS^o}	landing site azimuthal angle for a spherical coordinate system, (º)
ρ	Mars atmospheric density, (kg/m^3)
θ	polar angle for a spherical coordinate system, (º)
θ_{LS^o}	landing site polar angle for a spherical coordinate system, (º)
ω	argument of perigee, (º)
ω_m	Mars rotational rate, (rad/s)
μ_M	Mars gravitational parameter, (m^3/s^2)
μ_m	Moon gravitational parameter, (m^3/s^2)
v	true anomaly, (º)

CHAPTER 1
INTRODUCTION

1.1 Problem Statement

The long-term goal of NASA's space exploration program is to achieve safe and precise landing, where the challenges from the perspective of the entry, descent and landing **(**EDL) study involve works encompassing complex, hazardous terrain patterns and atmospheric uncertainty such as Mars' atmosphere [1 – 3]. The EDL system is classified as a critical mission component for NASA, where support technologies must demonstrate the ability to perform any or all three mission phases successfully. According to NASA's roadmap TA 9 draft, EDL technologies cover a spectrum of studies devoted to systems hardware, operations and simulating scenarios that will fulfill the desired mission goals [4]. Due to the limited range of testing conditions and the high cost to conduct experimental tests, the EDL Modeling and Simulation (M&S) capabilities are highly valued and utilized in each phase for mission design and analysis. This allows for development of physical models, numerical methodologies, software tools and experimental validation. Current M&S technology can accurately conduct steady aerodynamic analysis of rigid configurations. However, predictive capabilities for the entry and descent phase are inadequate where system hardware tends to undergo excessive design leading to complicated or unnecessary degrees of capability. The next generation of EDL systems will rely on robust and efficient simulation capabilities to improve and capture complex flows of larger payloads in order to accurately define system design, margins and reliability [5].

1.2 The Challenges of Precise Landing

NASA's focus to advance space exploration has necessitated further development to improve current capabilities while overcoming technical challenges. Mars being the most similar planet to Earth, has captivated scientists and remains a top priority in NASA's space exploration program [6]. However, landing a spacecraft on the surface of Mars is one of the most difficult challenges for robotic and human missions. Several factors include safely removing the lander's kinetic energy while providing the necessary technological capabilities that will work in favor with Mars' atmosphere and terrain [2,3]. Majority of today's developments in fundamental EDL technologies are derived from missions performed in the 1960s and 1970s [7]. In particular,

results and analysis from the Mars Viking Program (1970) is heavily utilized as the foundation for incorporating added complexities in hopes of accomplishing scientific return [8, 9]. Majority of the technologies from the Apollo missions served as reference design in the Orion crewed exploration vehicle where the design was extended to three times its original volume [10]. However, heavy reliance on heritage technologies will continue to constrain and pose limitations to achieving NASA's core science goals and future missions to distant planets.

1.3 Precise Landing and Future Sample Return Missions

While NASA has been involved in unmanned robotic landings on Mars and sample return missions such as JAXA's HAYABUSA, Genesis and Stardust, the United States has not attempted a sample return mission from the Moon since the Apollo program [11]. Therefore, the international Mars Architecture for the Return of Samples (iMARS) was chartered in 2006 to develop an outlined plan of the scientific and engineering requirements for carrying out a Mars sample return mission [12]. In addition, the development of a comprehensive sample return mission architecture has been prioritized and recommended by the 2012 National Research Council (NRC) Decadal Survey [13]. Future sample return missions will include unprecedented complexities, requiring advanced trigging events during the EDL maneuver to achieve safe and precise landing for maximizing the scientific return. Performing precise landing for sample return missions becomes critical in the overall mission timeline since landing closer to scientific areas of interests decreases the travel time to and from the designated landing site and maximizes the sample acquisition process to ensure quality samples are collected.

Sample return missions to the Moon and Mars have become a high priority because the poles of the Moon contain volatile reservoirs, useful for resource extraction and Mars is the most Earth-like planet in the solar system, where the early history of Earth's existence could be potentially revealed [12, 14]. Since the Apollo program ended in 1972, new discoveries involving the Moon's geological processes and evolution provide a unique opportunity for planetary scientists to reinvestigate potential solutions in deciphering the origins of the solar system. The Apollo crewed missions heavily focused on target landing sites within the vicinity of the Moon's equator, leaving other areas of the Moon unexplored. However, recent lunar robotic missions such as Clementine, Lunar Prospector, Chandrayaan-1 and Lunar Crater Observation and Sensing Satellite (LCROSS) have revealed deposits of hydrogen and water-ice located at the south and probably north poles of the lunar surface [15 – 17]. In 2018, direct

evidence of ice on the Moon's surface was validated by the findings of near-infrared water absorption features in Chandrayaan-1's Moon Mineralogy Mapper (M^3) data [18]. Although in-situ probe data and critical information can be retrieved through measurements recorded by a rover or satellite, a returned sample to Earth will be exposed to cutting-edge technologies and laboratories that can carefully analyze samples within a controlled environment. Therefore, the next generation of EDL capabilities will have to accommodate for specialized sample acquisition instrumentation while improving the landing accuracy to desired locations.

1.4 Improving the Landing Accuracy for Mars Missions Over Time

The EDL system from previous successful Mars missions consisted of a high-drag heat shield and parachute to remove 99.98 percent of the kinetic energy. Three generations of additional landing technologies were incorporated to remove the remaining kinetic energy and increase the overall landing accuracy [2]. The following illustration (Fig. 1.1) includes a landing ellipse for Mars 1976 Vikings, 1997 Pathfinder, 2004 Opportunity and Spirit, 2008 Phoenix and 2012 Curiosity.

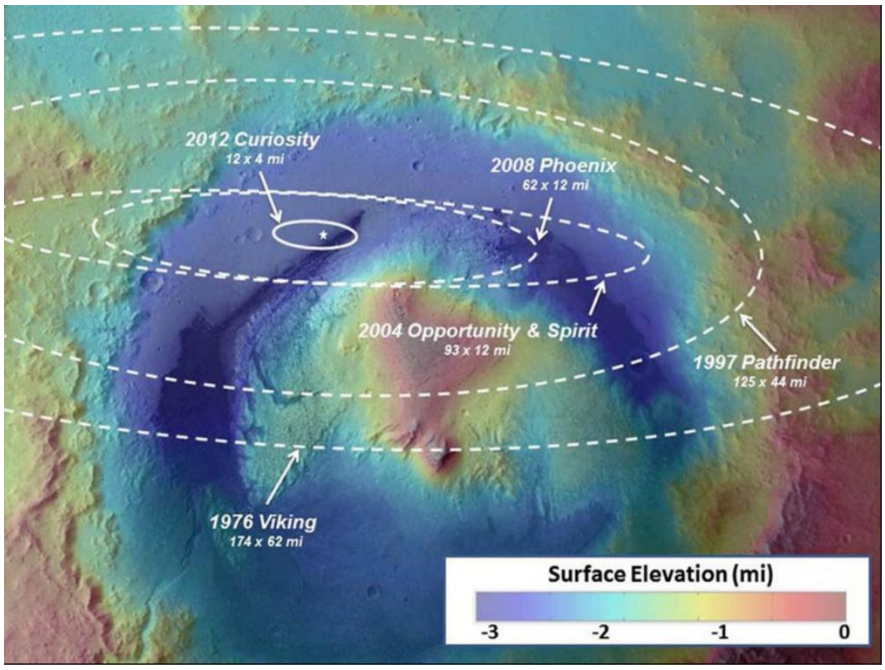

Figure 1.1: Landing Accuracy on Mars – A Historical Perspective [19].

The landing accuracy for the Mars Viking Program achieved a landing ellipse of 280 x 100 km while the Mars Pathfinder was 201 x 71 km. The Mars Exploration Rover (MER) mission successfully landed two rovers known as Spirit and Opportunity on January 4th and 25th of 2004,

respectively. According to the "Landing Targets and Requirements Table," the landing locations for both Spirit and Opportunity were within the pre-entry predictions of the landing target. That is 10 and 25 km, from the designated landing site [7]. The MER project's focus was to determine landing hazards and predict landing risks evaluated in real-time and updated for the navigation portion during the final stages of landing [20]. With the Phoenix mission, the landing accuracy had a slight decrease for a landing ellipse of 98 x 19 km in comparison to Spirit and Opportunity. The Mars Science Laboratory (MSL) mission, landed a robotic rover known as Curiosity in August 2012, where the results came out to be 20 by 6.5 km landing error relative to the landing target. For this mission, a closed-loop Guidance, Navigation and Control (GNC) system was implemented utilizing guided entry to reduce target errors during EDL [21]. Another recent mission known as InSight, occurred in November 2018 and landed within the proposed landing ellipse of 130 x 17 km where the spacecraft had 99 percent chance of landing at the center of the ellipse [22]. The current navigation and guidance technologies guarantees safe landing; however, accuracy of landing from kilometers to meters is still an ongoing problem. There are numerous studies devoted to reference trajectory optimization, where the constructed entry trajectory has a preplanned landing scenario which is further discussed in the following subsection.

1.5 Prior Art and Current Studies in Trajectory Optimization

The off-line reference trajectory generation is determined before a mission where the primary goal is to develop an optimal trajectory under a set of complex constraints [6]. Recent works have proposed intelligent global searching methods to solve the trajectory optimization problem. Particle swarm optimization techniques have been considered for defining the guidance history and configuration for each flight regime or to improve the overall computational cost [23, 24]. While hybrids of stochastic search tools, such as genetic algorithms, focused on specified constraints such as dynamic pressure, heat flux, entry flight path angle, bank angle and fixed parachute deployment conditions [25 – 27]. These studies solely considered the overall safety of the mission, where altitude and velocity at parachute deployment were emphasized. However, to further develop the technology for Mars landing will involve improving the disturbances on the dynamical model and observability of the navigation system.

Several researchers and mission designers have devoted their efforts towards improving the on-line trajectory generation model which accounts for uncertainties in the EDL dynamical model, aerodynamic conditions, varying atmospheric densities and the low control authority of

the lander. The on-line trajectory generation method assumes that all conditions, constraints and nominal equations of motion are satisfied within the design space. Soler et al. (2013) developed a trajectory generation method by proposing a planning scheme using the parameterization of bank angle profile. While Duan et al. (2016) implemented a guidance tracking/replanning algorithm where the on-board system computes the switching times for the bank profile while updating the drag profile. Although limited, these studies account for both safe landing and accuracy. Therefore, the proposed research aims to develop a reliable and computationally acceptable model that considers both safe and precise landing that will contribute to future missions.

1.6 Thesis Outline

To improve the overall accuracy of landing, this study aims to generate and construct trajectory envelopes using backward and forward propagation methods to minimize the landing error while achieving NASA's mission goals.

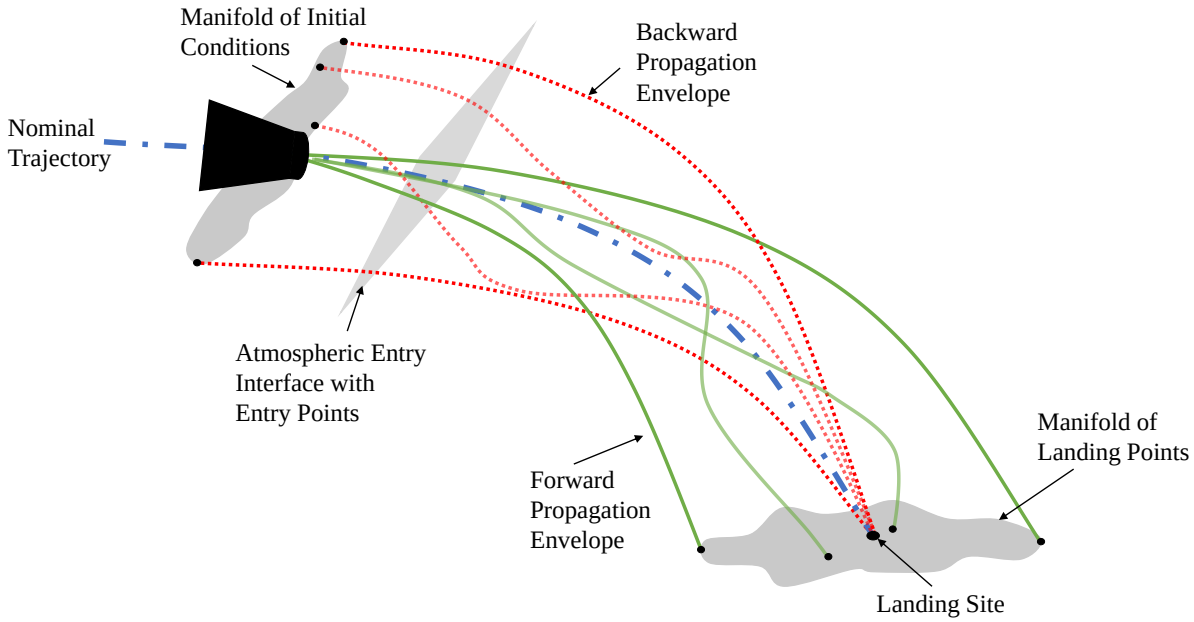

Figure 1.2: Illustration of EDL maneuver with backward and forward propagation trajectory envelopes.

Fig. 1.2 illustrates a cylinder-shaped envelope formed by the manifolds of the entry and landing conditions based on the lander's state. Two different envelope approaches are displayed in the figure to compare with the nominal trajectory. The backward propagation method begins at the designated landing site and completes the maneuver at an arbitrary point in the space of the Martian atmosphere (red curves). This work heavily utilized the forward propagation method,

where the integration begins at a point in space and descends into the Martian atmosphere (green curves). The final condition is then achieved within the vicinity of the designated landing site. Early developments of this work included creations of trajectory envelopes using both methods separately, where the dynamical model consisted of continuous thrust throughout the entire maneuver [30, 31]. This study incorporated two additional phases (events) to complete the EDL maneuver and summarized them as follows: exoatmospheric thrust phase, atmospheric transit phase and powered descent and landing phases. Each of these phases are connected using the continuity conditions of the lander's state vector at the junction points, where the lander's position and velocity vectors are continuous [32, 33]. The dynamical models for each phase utilize parameters and conditions from previous Mars missions, such as desired ranges of rocket performance parameters, Mars atmospheric conditions with varying density in relation to altitude and varying thrust direction angles of the lander. However, the dynamical model for the atmospheric transit phase has been simplified by excluding fixed parachute deployment conditions. In addition, a rudimentary study was conducted for lunar powered descent and ascent maneuvers, where the dynamical model and desired initial conditions were derived at the later stages of this work or the development of synthesized EDL trajectories.

To improve the overall accuracy of landing, this work aims to generate and construct trajectory envelopes to minimize the landing error while achieving the mission goals [34, 35]. The main objectives of this research are to (1) achieve a velocity magnitude v of less than 1 m/s upon touchdown and an altitude h of ±5 m (2) minimize fuel consumption and (3) achieve a landing accuracy of 100 m (4) achieve a h of 15,000 m for the lunar ascent maneuver. Fig. 1.3 summarizes the desired ranges of altitude, velocity and time for each phase of the entire EDL maneuver.

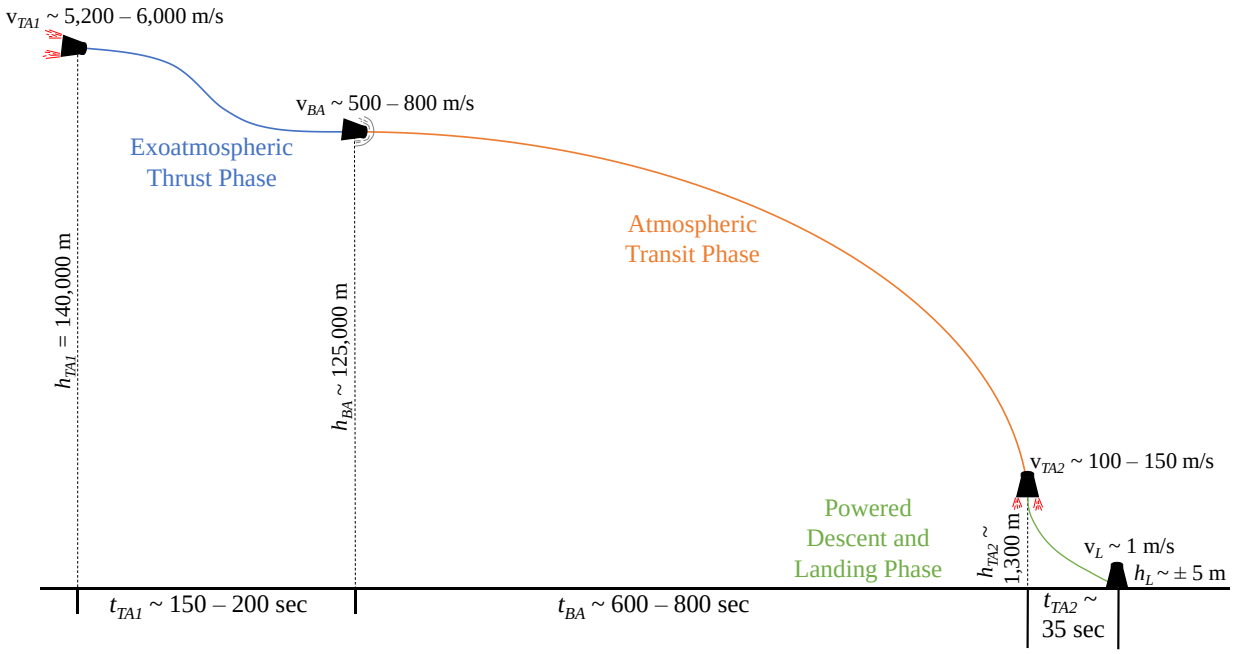

Figure 1.3: EDL profile describing the desired ranges of *h*, v and time for all three phases.

In this paper, the landing accuracy is measured as the distance between the actual and designated landing points. Based on the preliminary simulations, one can review the behavior of the state vector components to design the phases along a feasible EDL trajectory using backward and forward integration methods for planetary missions. The following sections will describe the approach and model used to generate the proposed trajectories.

CHAPTER 2
TRAJECTORY AND LANDING PROBLEM

Conducting landing trajectory analysis involves the development of envelopes and manifolds to be utilized for investigating feasible solutions to the precision landing problem. With the creation of diverse variations for entry and landing site conditions, one can generate multiple manifolds of points to reduce the landing error of trajectories. This research considers backward and forward propagation to simulate the three phases of the proposed EDL maneuver for Mars and lunar missions. The trajectory envelope model consists of the Newtonian equations of motion with additional components including varying the error term thrust angles, ($\Delta\alpha$, $\Delta\beta$, $\Delta\gamma$) and atmospheric drag acceleration, **D**. The additional components were selected accordingly at certain stages of the EDL maneuver.

Throughout this paper, the three phases are notated as follows: the exoatmospheric thrust phase is "thrust arc 1", *TA1*, the atmospheric transit phase is "ballistic arc", *BA*, and the powered descent and landing phase is "thrust arc 2", *TA2*. While the lunar descent and ascent phase is *LD* and *LA* respectively. Fig. 2.1 displays an overview of the spherical coordinate system and the lander's path along the EDL maneuver, where r is the radial distance from the center of Mars to the designated landing site (θ, ϕ) in spherical coordinates and x, y and z represent the position vector components of the lander's center of mass in cartesian coordinates.

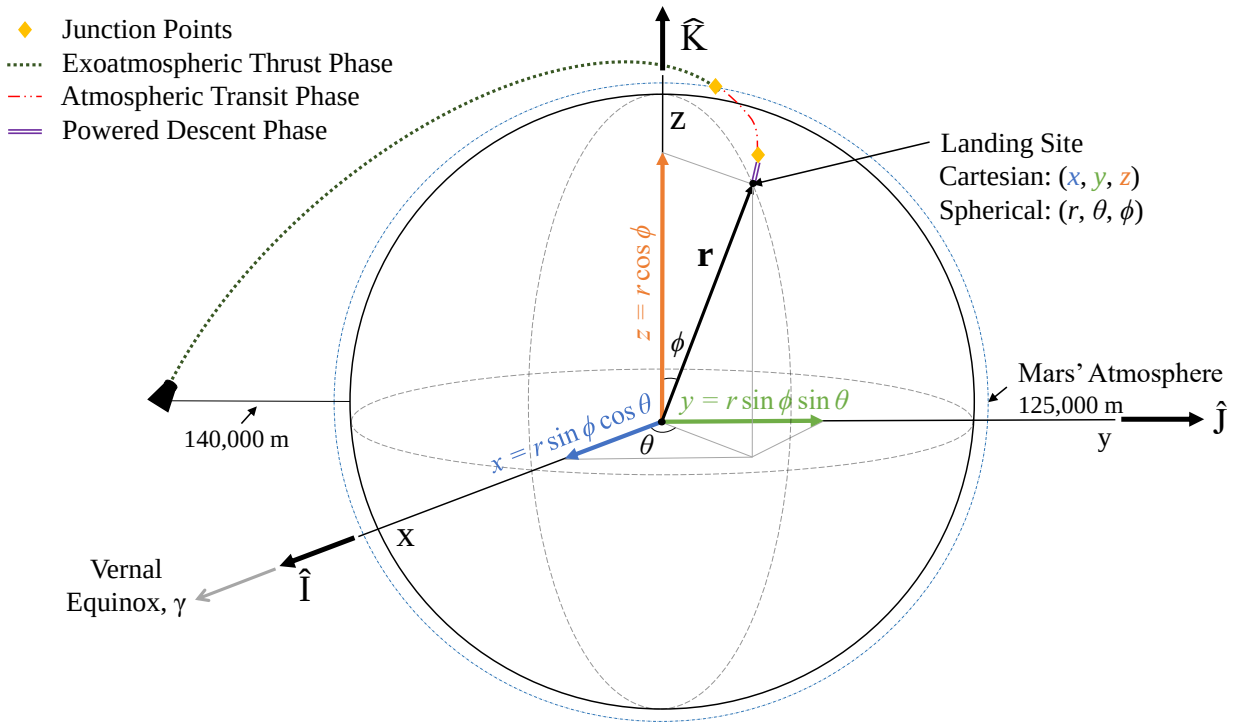

Figure 2.1: Lander along the EDL maneuver with its respective phases and cartesian coordinate system.

2.1 Equations of Motion for EDL Maneuver

Each of the three phases are executed using a specific set of systems of equations of motion throughout the entire EDL maneuver. The exoatmospheric thrust phase is given in the following form:

$$\dot{x}_{TA1} = \mathrm{v}_{x\text{-}TA1} \tag{2.1}$$

$$\dot{y}_{TA1} = \mathrm{v}_{y\text{-}TA1} \tag{2.2}$$

$$\dot{z}_{TA1} = \mathrm{v}_{z\text{-}TA1} \tag{2.3}$$

$$\ddot{x}_{TA1} = -\frac{\mu x_{TA1}}{{r_{TA1}}^3} + \frac{c_{TA1}\dot{m}_{TA1}}{m_{TA1}}\cos\alpha \tag{2.4}$$

$$\ddot{y}_{TA1} = -\frac{\mu y_{TA1}}{{r_{TA1}}^3} + \frac{c_{TA1}\dot{m}_{TA1}}{m_{TA1}}\cos\beta \tag{2.5}$$

$$\ddot{z}_{TA1} = -\frac{\mu z_{TA1}}{{r_{TA1}}^3} + \frac{c_{TA1}\dot{m}_{TA1}}{m_{TA1}}\cos\gamma \tag{2.6}$$

$$m_{TA1} = m_{0\text{-}TA1} - \dot{m}_{TA1}t_{TA1} \tag{2.7}$$

where v_x, v_y and v_z are the velocity components of the lander, μ_M is Mars' gravitational parameter, t is the time, c is the exhaust velocity, $\dot{m}$ is the mass flow rate, m_0 and m is the initial

and current masses of the lander and $cos\,\alpha$, $cos\,\beta$ and $cos\,\gamma$ are the thrust direction cosines. Fig. 2.2 displays the lander's relationship between its velocity vector and thrust direction cosines.

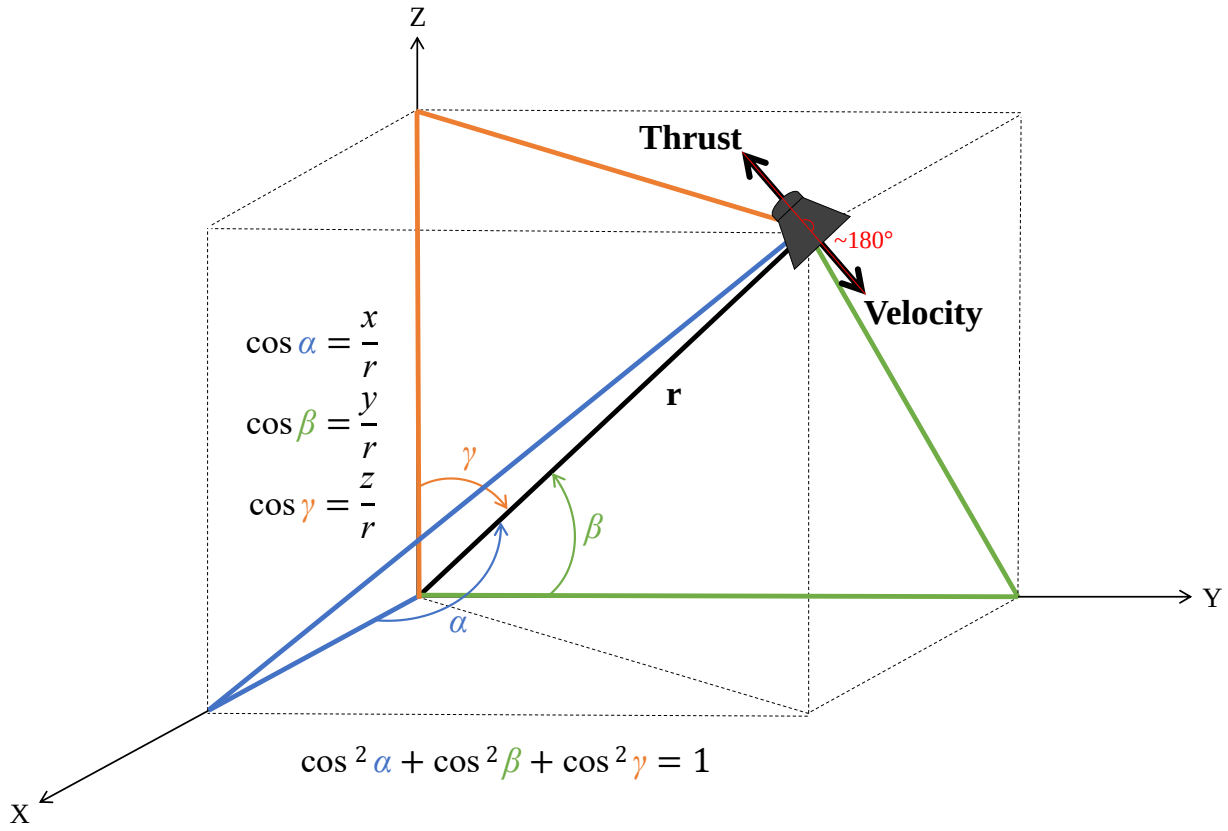

Figure 2.2: Thrust direction cosines and velocity vector of the lander.

This model is also used for the lunar descent and ascent maneuvers. While the atmospheric transit phase,

$$\dot{x}_{BA} = v_{x\text{-}BA} \tag{2.8}$$

$$\dot{y}_{BA} = v_{y\text{-}BA} \tag{2.9}$$

$$\dot{z}_{BA} = v_{z\text{-}BA} \tag{2.10}$$

$$\ddot{x}_{BA} = -\frac{\mu x_{BA}}{r_{BA}^3} + D_{x\text{-}BA} \tag{2.11}$$

$$\ddot{y}_{BA} = -\frac{\mu y_{BA}}{r_{BA}^3} + D_{y\text{-}BA} \tag{2.12}$$

$$\ddot{z}_{BA} = -\frac{\mu z_{BA}}{r_{BA}^3} + D_{z\text{-}BA} \tag{2.13}$$

includes the atmospheric drag components D_x, D_y and D_z. Finally, the powered descent and landing phase, incorporates the gravitational, thrust and drag acceleration components in Equations (2.18) – (2.20) [36].

$$\dot{x}_{TA2} = \mathrm{v}_{x\text{-}TA2} \tag{2.14}$$

$$\dot{y}_{TA2} = \mathrm{v}_{y\text{-}TA2} \tag{2.15}$$

$$\dot{z}_{TA2} = \mathrm{v}_{z\text{-}TA2} \tag{2.16}$$

$$\ddot{x}_{TA2} = -\frac{\mu x_{TA2}}{r_{TA2}^{\,3}} + \frac{c_{TA2}\dot{m}_{TA2}}{m_{TA2}}\cos\alpha + D_{x\text{-}TA2} \tag{2.17}$$

$$\ddot{y}_{TA2} = -\frac{\mu y_{TA2}}{r_{TA2}^{\,3}} + \frac{c_{TA2}\dot{m}_{TA2}}{m_{TA2}}\cos\beta + D_{y\text{-}TA2} \tag{2.18}$$

$$\ddot{z}_{TA2} = -\frac{\mu z_{TA2}}{r_{TA2}^{\,3}} + \frac{c_{TA2}\dot{m}_{TA2}}{m_{TA2}}\cos\gamma + D_{z\text{-}TA2} \tag{2.19}$$

$$m_{TA2} = m_{0\text{-}TA2} - \dot{m}_{TA2}t_{TA2} \tag{2.20}$$

2.2 Atmospheric Drag Acceleration

The atmospheric drag acceleration, **D** vector is defined by the equation,

$$\mathbf{D} = -\frac{1}{2}\rho \mathrm{v}_{rel}\left(\frac{C_D A}{m}\right)\mathbf{v}_{\boldsymbol{rel}} \tag{2.21}$$

where ρ is Mars' atmospheric density, C_D is the drag coefficient of 1.7, A is the front area of the spacecraft of 5.52 m^2 and the relative velocity, $\mathbf{v}_{\boldsymbol{rel}}$ is given as

$$\mathbf{v}_{\boldsymbol{rel}} = \mathbf{v} - \boldsymbol{\omega_m} \times \boldsymbol{r}$$

where $\boldsymbol{\omega_m}$ is the Mars rotational rate vector with magnitude of 7.0882 x 10^{-5} rad/s. The atmospheric conditions and drag model values were retrieved from [11].

2.3 Junction Point Parameters

The junction point parameters define the final conditions upon each of the three EDL phases. These results are obtained by the numerical integration of Equations (2.1) – (2.20). Note that a trajectory phase before the proposed EDL phases may belong to an interplanetary cruise, transfer or parking orbit. In the latter cases, the position and velocity of the lander in polar coordinates are r, u, v_r and v_f:

$$r = \frac{p}{1 + e\cos v} \tag{2.22}$$

$$v_r = \sqrt{\frac{\mu_M}{p}}\, e \sin v \tag{2.23}$$

$$v_f = \sqrt{\frac{\mu_M}{p}}\,(1 + e\cos v) \tag{2.24}$$

$$u = v + \omega \tag{2.25}$$

where p is the semi latus rectum, v is the true anomaly, v_r is the radial velocity component, v_f is the velocity normal to the position vector, u is the argument of latitude at epoch and ω is the argument of perigee [36].

2.4 Junction Point Conditions

The following conditions must be satisfied at the junction points between the proposed phases:

Junction 1 (at t_0):

$$r_{cruise} = r_{TA1(t_0)} \tag{2.26}$$

$$v_{r_{cruise}} = v_{r_{TA1(t_0)}} \tag{2.27}$$

$$v_{f_{cruise}} = v_{f_{TA1(t_0)}} \tag{2.28}$$

$$u_{cruise} = u_{TA1(t_0)} \tag{2.29}$$

Junction 2 (at t_1):

$$r_{TA1(t_1)} = r_{BA(t_1)} \tag{2.30}$$

$$v_{r_{TA1(t_1)}} = v_{r_{BA(t_1)}} \tag{2.31}$$

$$v_{f_{TA1(t_1)}} = v_{f_{BA(t_1)}} \tag{2.32}$$

$$u_{TA1(t_1)} = u_{BA(t_1)} \tag{2.33}$$

Junction 3 (at t_2):

$$r_{BA(t_2)} = r_{TA2(t_2)} \tag{2.34}$$

$$v_{r_{BA(t_2)}} = v_{r_{TA2(t_2)}} \tag{2.35}$$

$$v_{f_{BA(t_2)}} = v_{f_{TA2(t_2)}} \tag{2.36}$$

$$u_{BA(t_2)} = u_{TA2(t_2)} \tag{2.37}$$

Junction 4 (at t_3):

$$r_{TA2(t_3)} = r_{planet} \tag{2.38}$$

$$v_{r_{TA2(t_3)}} = 0 \tag{2.39}$$

$$v_{f_{TA2(t_3)}} = 0 \tag{2.40}$$

$$u_{TA2(t_3)} = u_{LS} \tag{2.41}$$

Note that the last junction point is considered as the landing point. Each junction satisfies the initial conditions of the subsequent phase, based on the final conditions computed from the prior phase.

2.5 Manifold of landing points and accuracy

A landing ellipse (or circle) consists of a manifold of landing points where a specific coordinate system can be defined in two or three dimensions. A two-dimensional manifold is a family of landing points generated by specified entry velocity parameters in the *x* and *z* direction of the cartesian coordinate system. While the three-dimensional manifold incorporates another parameter in the *y* direction. For simplicity, this study models scenarios in two dimensions. There are two landing points that are significant to creating a manifold, the furthest and closest point to the designated landing site. The accuracy of landing is defined by the cross-track distance, d between the designated landing site (x_{LS}, y_{LS}) to the landing point of interest (x_T, y_T) is expressed as:

$$d = \sqrt{(x_{LS} - x_T)^2 + (y_{LS} - y_T)^2}$$

where the desired cross-track distance is within 100 m. Fig. 2.3 displays a landing ellipse in three dimensions with a family of landing points within the vicinity of the designated landing site.

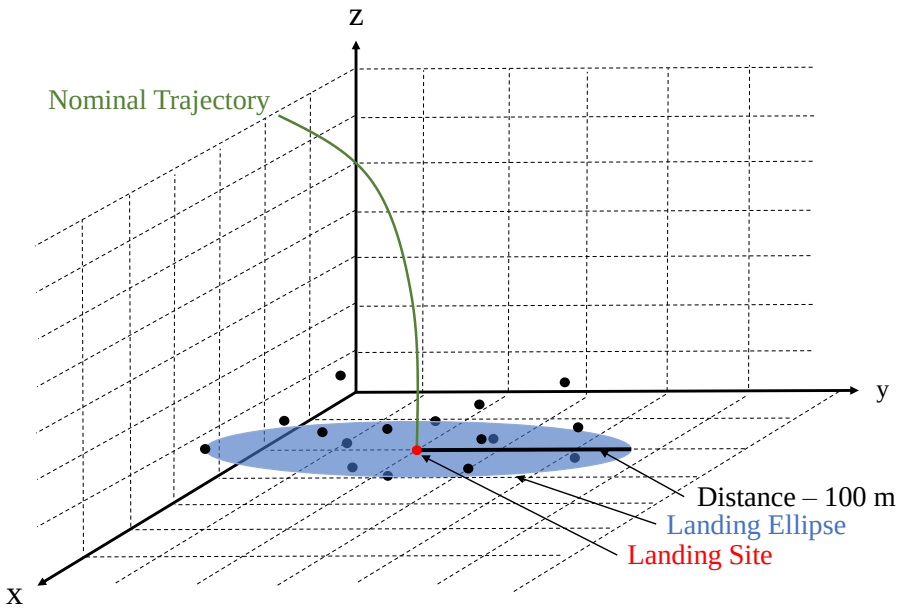

Figure 2.3: Manifold of landing points within a landing ellipse.

CHAPTER 3
METHODOLOGY

3.1 Backward State Propagation

Backward propagation is defined as beginning the integration sequence from the designated landing site and continuing the maneuver till the lander achieves the desired entry conditions. The initial parameters for the backward state propagations include specifying the final velocity magnitude v components and landing site coordinates (θ_{LS^0} and ϕ_{LS^0}). These were selected as arbitrary values while the position coordinates are expressed in the form of spherical coordinates: $x_{LS} = Req \sin\phi_{LS^0}\cos\theta_{LS^0}$, $y_{LS} = Req \sin\phi_{LS^0}\sin\theta_{LS^0}$ and $z_{LS} = Req \cos\phi_{LS^0}$ where Req is the equatorial radius of Mars. This method was used to validate the conditions and ranges specified in the forward propagation study where a significant portion of the results is devoted to this method.

3.2 Forward State Propagation

In contrast, the forward propagation method is defined as beginning the integration sequence from the atmosphere till touchdown of the Martian surface. The entry velocity components were obtained through trial and error in the initial stages of this work along with adjusting the lander's rocket performance parameters and error term thrust angles. This provided favorable results that were utilized to generate each EDL phase with their respective set of trajectory envelopes along with the results for the lunar descent and ascent maneuvers.

3.3 Thrust Direction

The thrust direction is determined based on the concept of minimization of the total energy, E [37]. The total specific energy of the lander is given as

$$E = \frac{1}{2}\mathrm{v}^2 - \frac{\mu}{r} \tag{3.1}$$

and its reference with respect to time is

$$\frac{dE}{dt} = \frac{c\dot{m}}{m}\mathrm{v}\cos\xi\,, \tag{3.2}$$

where $\xi = \angle(\hat{\lambda}_v, \mathrm{v})$ and $\hat{\lambda}_v$ is the thrust unit vector. The ranges can be determined as $\xi \subseteq \left(0, \frac{\pi}{2}\right) \subseteq \left(\frac{\pi}{2}, \frac{3\pi}{2}\right)$. For $\xi = \pi$, the following expression:

$$\frac{\partial}{\partial \xi}\left(\frac{dE}{dt}\right) = \frac{c\dot{m}}{m} \mathrm{v} \sin \xi \tag{3.3}$$

results in $\frac{\partial}{\partial \xi}\left(\frac{dE}{dt}\right) = 0$. When $\xi = \pi$, the energy rate can achieve its extremum with respect to the thrust direction. In this case, the thrust direction is opposite to **v** regardless of the thrust magnitude. The total energy is minimized at a maximum rate if $\xi = \pi$. Therefore, in this paper it will be assumed that the thrust direction remains approximately opposite to the velocity vector with minor deviation during the exoatmospheric and powered descent and landing phase [38]. The following section will describe the range specification for such deviation of the lander's thrust angle.

3.4 Varying Thrust Angle

In Reference 39, T. L. Yang developed a trajectory profile comparing two approaches known as the bilinear tangent and sine-cosine steering where deviation of the pitch angle demonstrates optimality at the ignition and final stage of EDL. Although these approaches demonstrated trajectory optimization, this did not provide any potential targeting solutions [39]. Thus, this study considers a linear numerical approximation where increased accuracy can be accomplished if the total thrust angle is very small [40]. According to Gilyard and Bolonkin (2000), for a nominal descent with a flight path angle, γ of -3º, a minimum thrust condition is achieved when the thrust-vectoring angle, η is approximately 0.8º [41]. Fig. 3.1 displays a free body diagram of the lander where the thrust-vector angle is varied within a small range and the corresponding error terms are described with respect to the cartesian coordinate system.

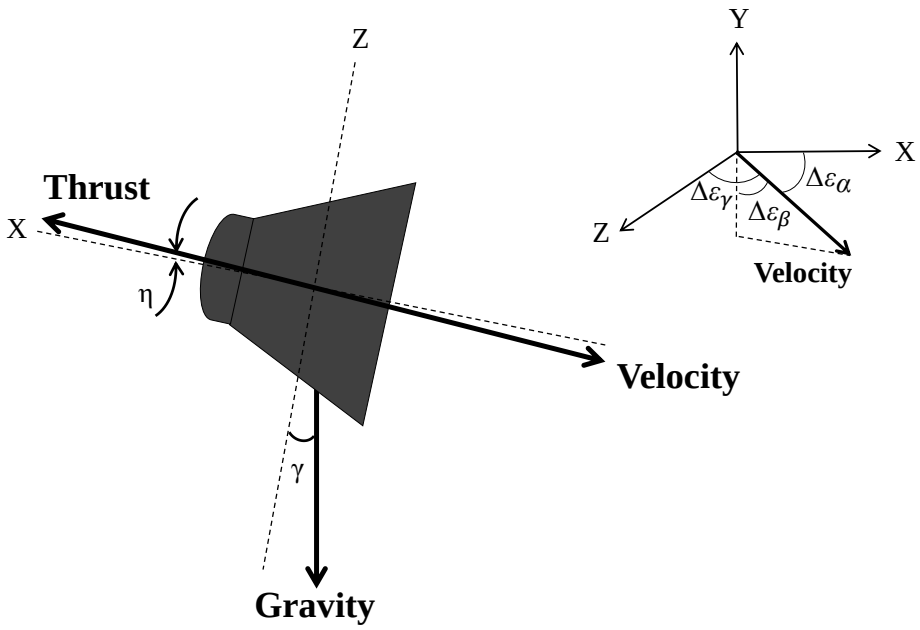

Figure 3.1: Free body diagram of the lander with varied thrust-vector angle.

The cosine direction angles ($cos\,\alpha, cos\,\beta, cos\,\gamma$) include an additional error term ($\Delta\varepsilon_\alpha$, $\Delta\varepsilon_\beta$, $\Delta\varepsilon_\gamma$) where the total thrust angle is within the proposed design space:

$$\cos\alpha = \frac{v_x}{v} + \Delta\varepsilon_\alpha\,, \tag{3.4}$$

$$\cos\beta = \frac{v_y}{v} + \Delta\varepsilon_\beta\,, \tag{3.5}$$

$$\cos\gamma = \frac{v_z}{v} + \Delta\varepsilon_\gamma \tag{3.6}$$

The simulations presented in this paper used fixed constants for $\Delta\varepsilon_\alpha$, $\Delta\varepsilon_\beta$, $\Delta\varepsilon_\gamma$ during the exoatmospheric thrust phase. Preliminary trade-off studies for trajectory behavior showed that varying $\Delta\varepsilon_\alpha$ and $\Delta\varepsilon_\gamma$ significantly impacted the duration, *t*, altitude, *h*, and velocity magnitude, *v*, during the maneuver. Therefore, an extensive analysis for adjusting the error terms was conducted throughout the course of this research for both the exoatmospheric and powered descent phase. The values were then finalized in the synthesizing of the EDL maneuver stage, lunar descent and ascent phase. This study specifies $\Delta\varepsilon_\alpha$ and $\Delta\varepsilon_\gamma$ as non-zero constants to achieve the primary precision landing goals.

3.5 Atmospheric Density Profiles

This study used the "Averaged Model", which is the average of the four atmospheric density profiles combined (red curve), to compute the drag force for the atmospheric transit and powered descent and landing phase.

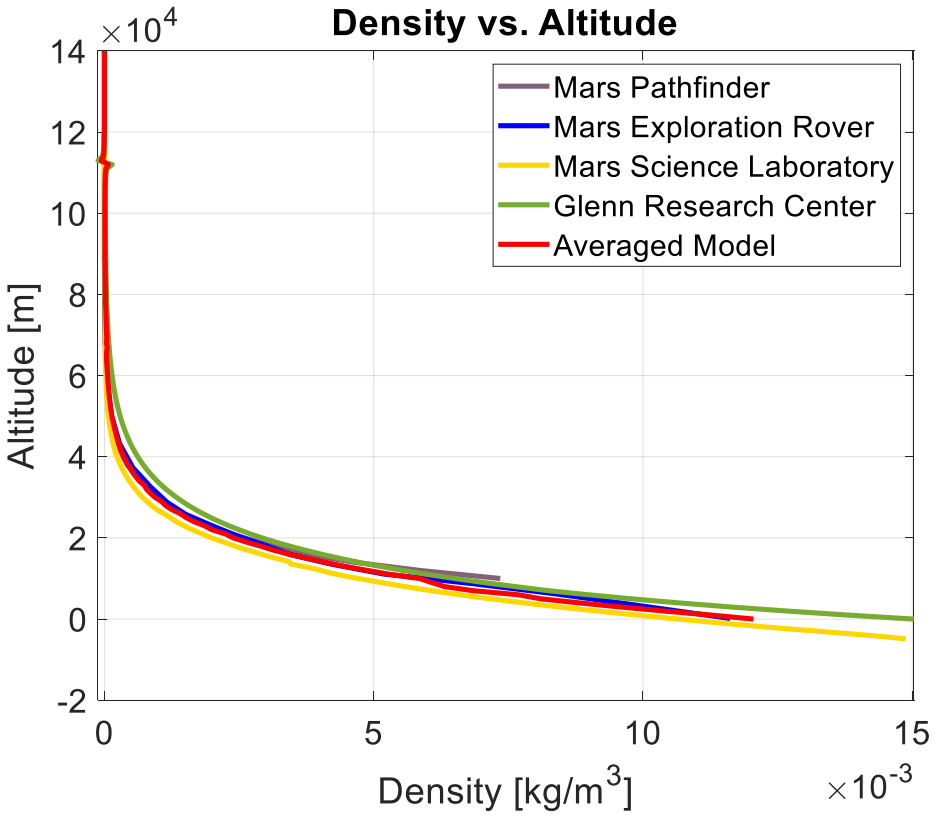

Figure 3.2: Density profiles from previous Mars missions [42, 43].

The density data was approximated and extracted from previous Mars missions that had specific goals and design considerations for their technological capabilities. The main purpose of this research is to develop a universal EDL maneuver for Mars missions of comprehensive applications. Previous studies from Reference 34 experimented with each model shown in Fig. 3.2, which revealed little to no effects on the behavior to the trajectories generated in MATLAB. Fig. 3.2 displays several density profiles from three missions: Mars Pathfinder, Mars Exploration Rover and Mars Science Laboratory with additional data contributed from Glenn Research Center [42, 43]. The reference surface on Mars at zero elevation is defined as the equipotential surface where the average value at the equator is equal to the mean radius of 3,389,508 ± 3 m, combined with a pressure surface of 6.105 millibars [44, 45].

CHAPTER 4
SYNTHESIS OF EDL TRAJECTORIES

The results presented in this section demonstrate trajectory envelopes representing different portions of the proposed EDL maneuver, synthesis of the three phases and lunar descent and ascent maneuvers for future mission design purposes. The following figures are presented independently as preliminary simulations (Fig. 4.1 and 4.2 (a) – (d)) from References 30, 31 and 46 using backward and forward propagation, the exoatmospheric thrust phase described in Fig. 4.3 (a) – (c), atmospheric transit phase described in Fig. 4.4 (a) – (b) and powered descent and landing phase described in Fig. 4.5 (a) – (c) from Reference 34. In addition, a synthesis of an EDL maneuver with junction point solutions (see in Fig. 4.6 – 4.8) that utilizes design parameters from previous missions while proposing specified initial rocket performance and thrust-vector angle values are results from Reference 34. Finally, the last subsections will describe trajectory envelopes for lunar descent and ascent maneuvers (Fig. 4.9 – 4.10) by varying the error term angles for thrust direction. Table 4.1 and 4.2 below summarize the planetary initial conditions for Mars and the Moon.

Table 4.1: Mars parameters.

Variable	Numeric Value
g_M	3.711 m/s^2
g_0	9.807 m/s^2
Req_M	3.3895 x 10^6 m
μ_M	4.2828 x 10^{13} m^3/s^2

Table 4.2: Moon parameters.

Variable	Numeric Value
g_m	1.62 m/s^2
g_0	9.807 m/s^2
Req_m	1.7371 x 10^6 m
μ_m	4.9049 x 10^{12} m^3/s^2

4.1 Backward Propagation for EDL Maneuver

The trajectory envelopes presented in Fig. 4.1 utilized the backward propagation method while undergoing continuous thrust from the prescribed landing site to a point in space. The initial conditions, landing site coordinates and rocket performance parameters denoted for this maneuver are summarized in Table 4.3.

Table 4.3: Initial conditions, landing site coordinates and rocket performance parameters representing Fig. 4.1.

Variable	Numeric Value
Isp_{BP}	220 sec
$m_{0\text{-}BP}$	2835 kg
$t_{i\text{-}BP}$	918.0 sec
$t_{f\text{-}BP}$	0.0 sec
T/W_{BP}	3
$v_{x\text{-}BP}$, $v_{y\text{-}BP}$, $v_{z\text{-}BP}$	-100 m/s
$\phi_{LS^o\text{-}BP}$	60º
$\theta_{LS^o\text{-}BP}$	30º

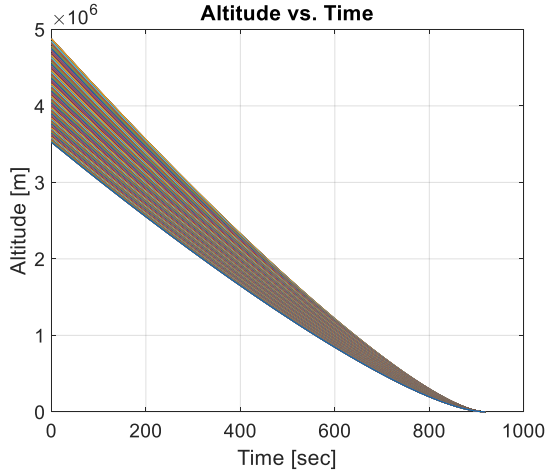

(a) Altitude vs. Time

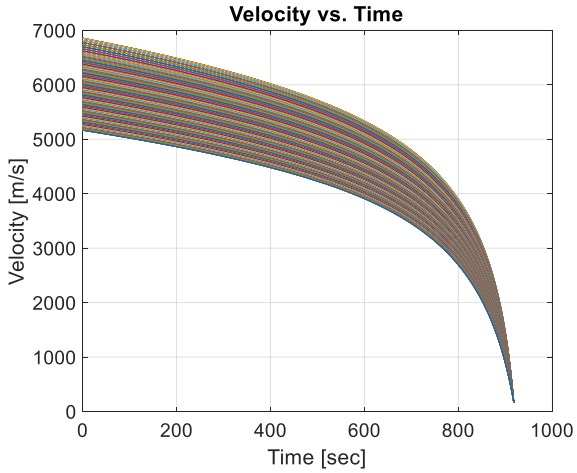

(b) Velocity vs. Time

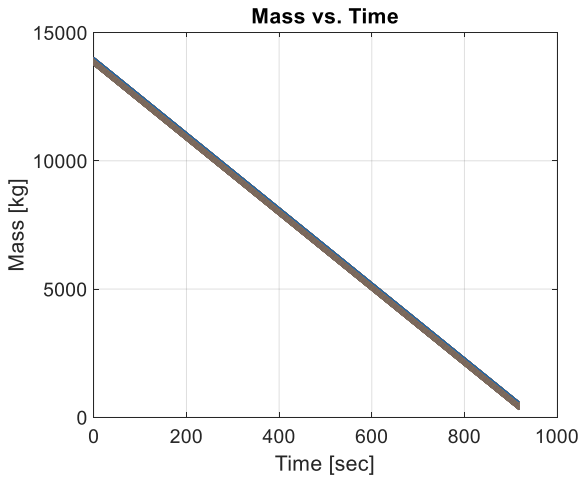

(c) Mass vs. Time

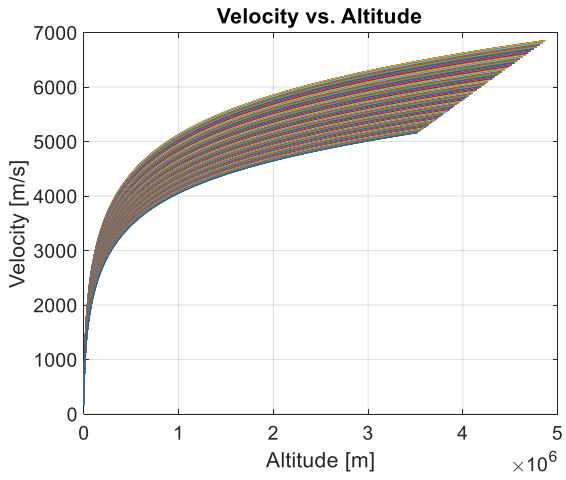

(d) Velocity vs. Altitude

Figure 4.1: Trajectory envelopes using backward propagation by varying $m_{0\text{-}BP}$ and $\theta_{LS^o\text{-}BP}$.

This envelope varied $m_{0\text{-}BP}$ and $\theta_{LS^o\text{-}BP}$ within an arbitrary range of 300 – 600 kg using an interval step size of 5 and 1º – 10º using an interval step size of 1 respectively. These results demonstrated that precise and safe landing is guaranteed when $\phi_{LS^o\text{-}BP}$, $\theta_{LS^o\text{-}BP}$ and $v_{x\text{-}BP}$, $v_{y\text{-}BP}$, $v_{z\text{-}BP}$ are specified. The initial rocket performance parameters and duration are adjusted to fulfill the boundary conditions of the proposed mission. Fig. 4.1 (a) portrays an increase in *h*, where the landing site begins at 0 m and achieves an *h* of approximately 3.5 x 10^6 – 4.9 x 10^6 m. In Fig. 4.1 (b), the v is 173.2051 m/s and ascends to roughly 5,100 – 6,900 m/s. In comparison with *h* and v, Fig. 4.1 (d) confirms that an increase in *h* corresponds to higher entry v. Fig. 4.1 (c) displays 11,200 kg of fuel is consumed over a duration of 918 sec. Although the preliminary precision landing requirements were achieved, continuous thrusting for the entire EDL maneuver is not efficient in terms of reducing fuel consumption. The overall duration used to generate the trajectory envelopes surpasses the ideal mission time of 7 min [11]. The following subsection will cover the same approach of utilizing continuous thrusting with the forward propagation method.

4.2 Forward Propagation for EDL Maneuver

The results presented in this subsection utilizes the forward propagation method where Fig. 4.2 describes trajectory envelopes undergoing continuous thrust from an arbitrary point in space and descends into the Martian atmosphere. Table 4.4 summarizes the initial conditions and landing site coordinates used to generate the simulation results displayed in Fig. 4.2.

Table 4.4: Initial conditions and landing site coordinates representing Fig. 4.2.

Variable	Numeric Value
$m_{0\text{-}FP}$	2451 kg
$t_{i\text{-}FP}$	0.0 sec
$v_{x\text{-}FP}$	4500 m/s
$v_{y\text{-}FP}$	0.0 m/s
$v_{z\text{-}FP}$	-2000 m/s
$\phi_{LS^o\text{-}FP}$	10º
$\theta_{LS^o\text{-}FP}$	0º

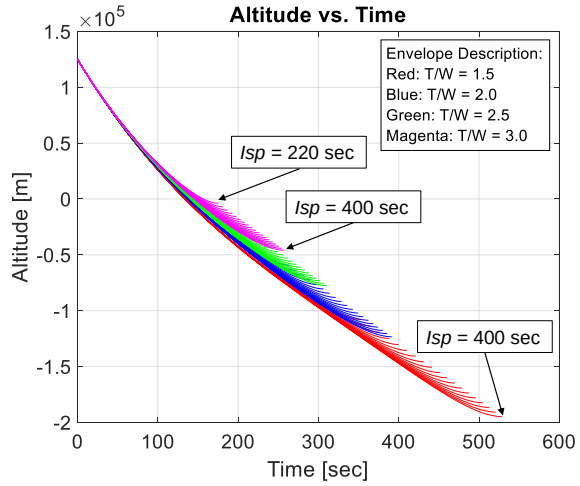

(a) Altitude vs. Time

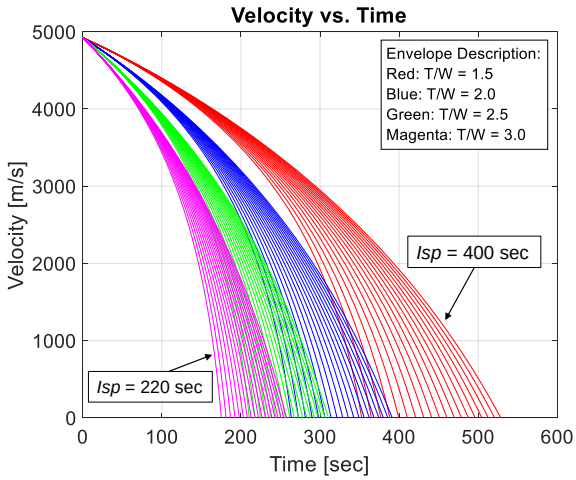

(b) Velocity vs. Time

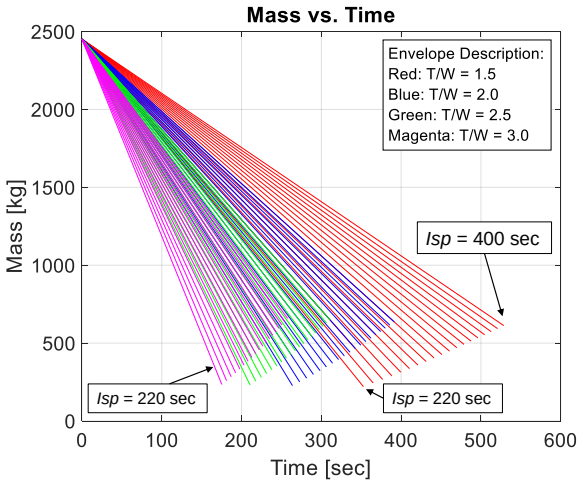

(c) Mass vs. Time

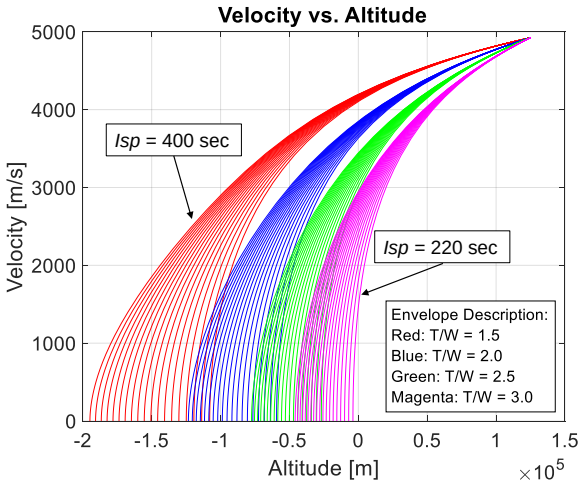

(d) Velocity vs. Altitude

Figure 4.2: Trajectory envelopes using forward propagation by varying *Isp* and *T/W*.

The trajectory envelopes were executed by varying the initial rocket performance parameters of *Isp* and *T/W*, where the desired ranges of 220 – 400 sec and 1.5 – 3 respectively were investigated [11]. To reduce the computation time, an interval step size of 10 for *Isp* and 0.5 for *T/W* were considered for this study. Fig. 4.2 (a) – (d) displays four colored trajectory envelopes representing different initial *T/W* values while varying *Isp*. For each trajectory envelope, the individual trajectory with the shortest duration used a *Isp* value of 220 sec and 400 sec for the longest duration. Fig. 4.2 (a) demonstrated that a trajectory with a *Isp* value of 220 sec and initial *T/W* value of 3 (upper magenta trajectory), achieved an *h* of 3.9216 x 10^3 m and spends approximately 180 sec to perform the maneuver. In Fig. 4.2 (b), the trajectories represented in

each envelope decelerated to 0 m/s which is also shown along the x-axis in Fig. 4.2 (d). Lastly, Fig. 4.2 (c) describes the rate of fuel consumption for different initial values of *Isp* and *T/W*. A significant amount of propellant is used with a *Isp* value of 220 sec, where a difference of 450 kg is conserved using a *Isp* of 400 sec. The trajectory envelopes described in this subsection, revealed that a *Isp* of 220 sec decelerates rapidly with a shorter duration than higher values of *Isp*. The lower initial values of *T/W* spend more time performing the maneuver and descending beyond the ideal *h* range for touchdown. In addition, reducing the amount of fuel consumed was achieved with a constant *Isp* of 400 sec. The analysis from this study was used to determine the three phases of the EDL maneuver individually using the forward propagation method discussed in subsections 4.3 – 4.5.

4.3 Exoatmospheric Thrust Phase

The exoatmospheric thrust phase maneuver begins at an *h* of 140,000 m where the lander descends to an *h* of 125,000 m (Mars atmosphere). The analysis that was conducted in subsection 4.2, was heavily utilized to investigate desirable ranges of initial conditions that will guarantee a lander's descent into Mars' atmosphere. Figure 4.3 displays trajectory envelopes based on the initial conditions and entry coordinates summarized in Table 4.5. The rocket performance parameters used 5 different scenarios of *Isp* varied at selected values of 220, 280, 320, 360 and 400 sec, while the initial *T/W* value for each case was specified as 3. The entry coordinates were determined through trial and error from the preliminary studies conducted in Reference 46.

Table 4.5: Initial conditions and entry coordinates representing Fig. 4.3.

Variable	Numeric Value
$m_{0\text{-}TA1}$	1000 kg
$t_{i\text{-}TA1}$	0.0 s
T/W_{TA1}	3
$v_{x\text{-}TA1}$	4906.2 m/s
$v_{y\text{-}TA1}$	0.0 m/s
$v_{z\text{-}TA1}$	-1097.5 m/s
$\phi_{LS^o\text{-}TA1}$	9.2º
$\theta_{LS^o\text{-}TA1}$	0º

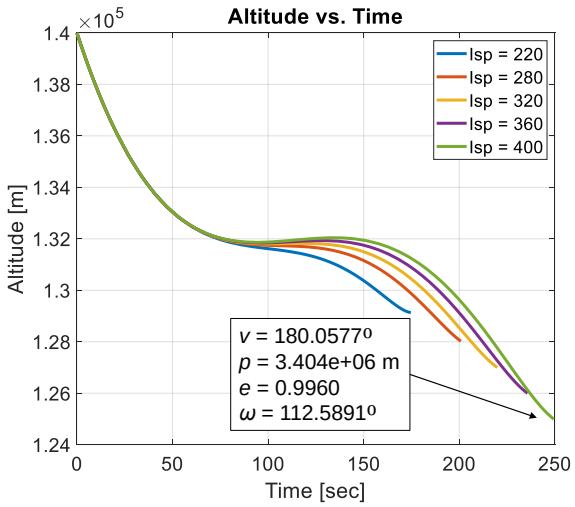

(b) Altitude vs. Time

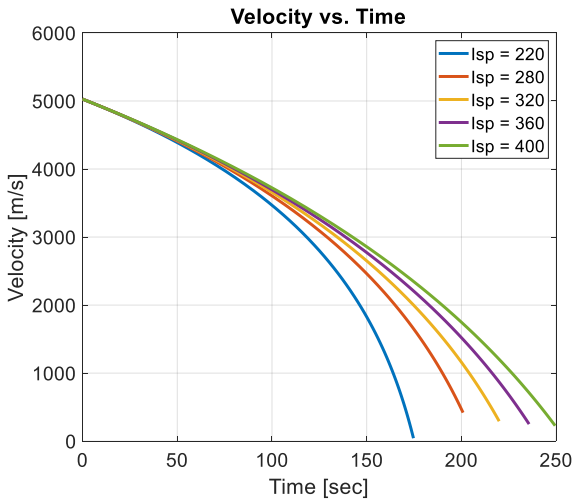

(b) Velocity vs. Time

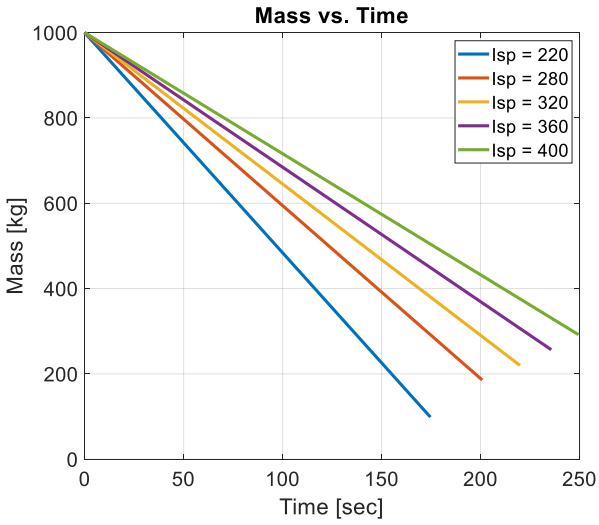

(c) Mass vs. Time

Figure 4.3: Trajectory envelopes using forward propagation for the exoatmospheric thrust phase varying *Isp.*

In Fig. 4.3 (a), the green trajectory with a *Isp* of 400 sec achieved an *h* of 125,000 m which allowed for determination of the junction point parameters. For Fig. 4.3 (b) and (c), the v at the junction point was approximately 227 m/s and the *m* was 292 kg over a duration of 249 sec. The period of the maneuver implies that the lander is performing indirect entry, where the spacecraft spends more time orbiting the body of interest while gradually descending and slowing down simultaneously [47]. The calculated junction point parameters summarized in the lower half of Fig. 4.3 (a) represent the lander traveling along a highly elliptical orbit. The test plots from the

earlier stages of this study showed that the initial *T/W* value of 3 with a *Isp* value of 400 sec, provided optimal and feasible results to achieve precise landing. Thus, the junction point parameters were determined since the desired initial rocket performance parameters met the primary precision landing requirements. The final conditions from each trajectory were extracted to compute the trajectory envelopes presented in subsection 4.4.

4.4 Atmospheric Transit Phase

The atmospheric transit phase maneuver begins at an *h* of 125,000 m (Mars atmosphere) where the lander descends until an *h* of 1,300 m is achieved [11]. Table 4.6 summarizes the atmospheric conditions used from the Curiosity mission [11] with the density profile derived from the "Averaged Model" (red curve) displayed in Fig. 3.2 of subsection 3.5.

Table 4.6: Atmospheric conditions representing Fig. 4.4.

Variable	Numeric Value
A	5.52 m^2
C_D	1.7
ω_m	7.0882 x 10^{-5} rad/s

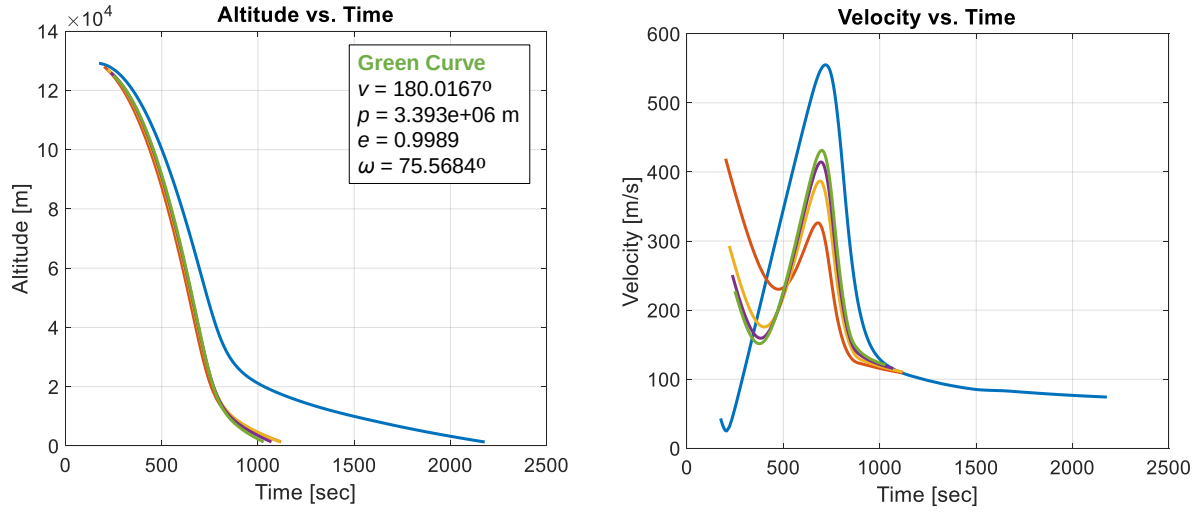

(a) Altitude vs. Time (b) Velocity vs. Time

Figure 4.4: Trajectory envelopes using forward propagation for the atmospheric transit phase.

Based on the final conditions presented in Fig. 4.3 (a), the blue, orange, yellow and purple curve begin the integration sequence where *h* is 129,000, 128,000, 127,000 and 126,000 m respectively. The trajectories displayed in Fig. 4.4 (a) achieved a final *h* of 1,300 m. Based on the

dynamical and atmospheric drag model described in Equations (2.8) – (2.13) and (2.21) respectively, the asymptotic behavior shown in Fig. 4.4 (b) portrays a numerical representation of the lander increasing v until optimal peak is achieved, then approaches terminal v after passing through Mars' atmospheric layers of varying density [48]. In Fig. 4.4 (b), the blue curve begins at a significantly low v and spends 2,000 sec to achieve an *h* of 1,300 m in comparison to the other trajectories. While the final v for the orange, yellow, purple and green curve range from approximately 110 – 120 m/s within 1,000 sec. Therefore, the final v components extracted from the exoatmospheric thrust phase directly impacts the overall duration of the maneuver during the atmospheric transit phase. To reduce the v while minimizing the duration of the maneuver, the initial v for the atmospheric transit phase must be greater than 400 m/s. The final *m* for each case from the exoatmospheric thrust phase remained a constant value throughout the entire maneuver. The final conditions from the atmospheric transit phase were collected to perform the powered descent and landing phase discussed in subsection 4.5.

4.5 Powered Descent and Landing Phase

The powered descent and landing phase initiates at an *h* of 1,300 m and must achieve a final *h* of ±100 m and v of less than 1 m/s. Table 4.7 provides the initial rocket performance parameters that were used to generate the trajectory envelopes presented in Fig. 4.5 (a) – (c). These parameters were specified assuming that the lander has deployed deceleration support technologies [49]. The final *m* from the exoatmospheric thrust phase (see in Fig. 4.3 (c)) is considered the initial *m* for the powered descent and landing phase where the final *t* was extracted from the atmospheric transit phase (see in Fig. 4.4 (a) and (b)) to construct the trajectories shown in Fig. 4.5 (a) – (c).

Table 4.7: Rocket performance parameters for powered descent and landing phase representing Fig. 4.5.

Variable	Numeric Value
Isp_{TA2}	400 sec
T/W_{TA2}	1.5

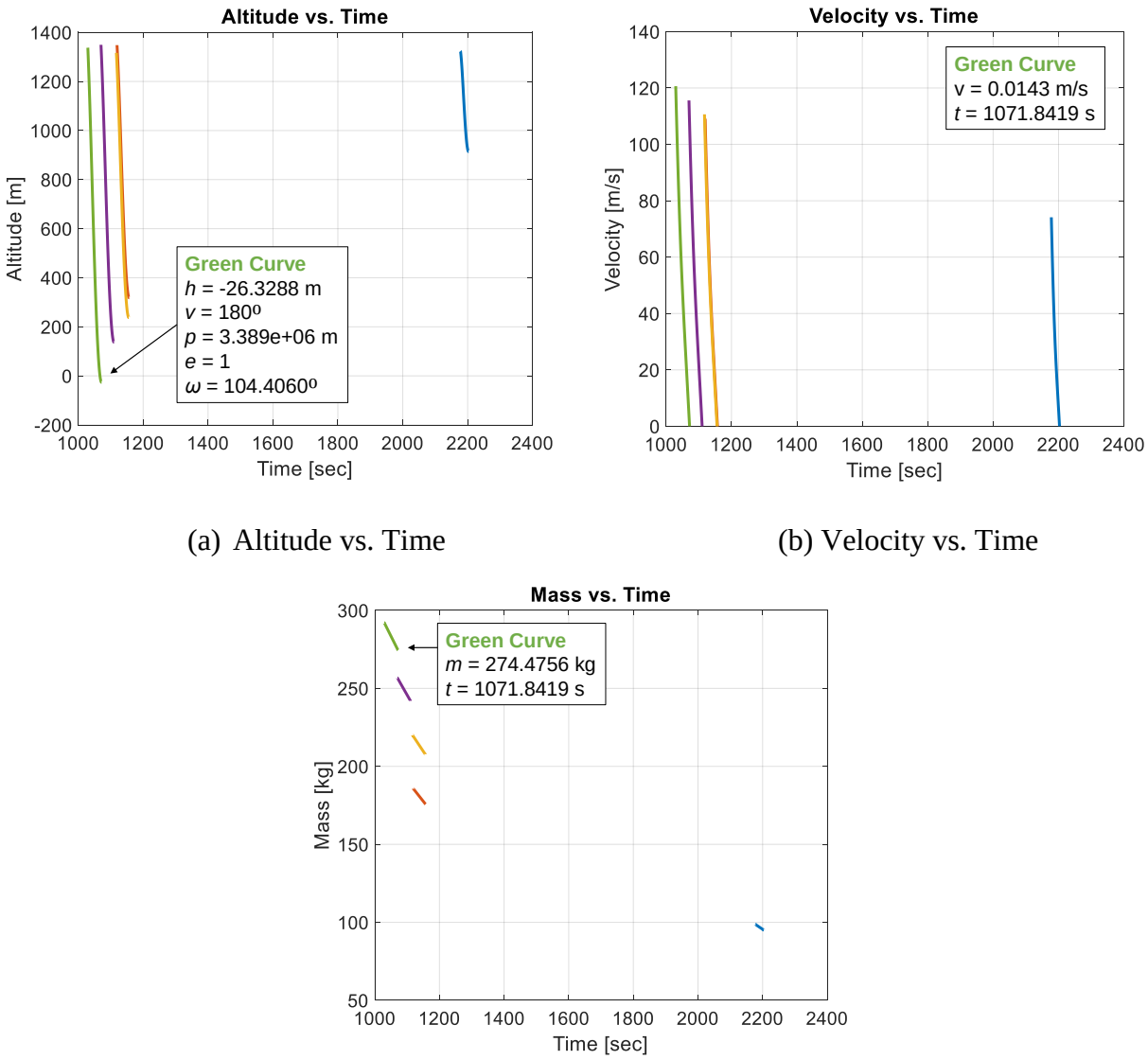

(a) Altitude vs. Time

(b) Velocity vs. Time

(c) Mass vs. Time

Figure 4.5: Trajectory envelopes using forward propagation for the powered descent and landing phase.

Figure 4.5 (a) – (c) represents the lander performing the final thrust maneuver as it descends to the surface of Mars. Fig. 4.5 (a) shows the green curve achieving an *h* of -26 m and summarizes the junction point parameters at a duration of 1072 sec. The final v for each trajectory is less than 1 m/s shown in Fig. 4.5 (b), however lower initial *Isp* values from Fig. 4.3 (a) – (c) demonstrates an increase in fuel consumption (see Fig. 4.5 (c)) and *h* from the Martian surface. In Fig. 4.5 (c), each curve displays a short duration of expending propellant to slow the lander down to zero velocity (see in Fig. 4.5 (b)). The duration of the blue curve in Fig. 4.5 (c) is a result of achieving a v of 80 m/s shown in Fig. 4.4 (b) in comparison to the other curves which portrays higher final

v values during the atmospheric transit phase. Thus, longer duration is required to perform the maneuver to achieve a v of less than 1 m/s. The dry *m* for the blue curve is approximately 90 kg in comparison to the green curve which is 274 kg respectively, where larger dry mass is desired for future sample return missions. Therefore, the green curve was selected for junction point determination since the initial parameters specified fulfilled two critical precision landing requirements which is within an *h* range of ±100 m and v of less than 1 m/s. The following subsection will combine all three phases to form the entire EDL maneuver that provides a solution to reduce the duration of the mission.

4.6 Synthesis of EDL Maneuver

The synthesis of the EDL maneuver is the connection of all three trajectory arcs formed by the exoatmospheric thrust, atmospheric transit and powered descent and landing phase as shown in Figure 4.6 (a) – (d). Fig. 4.3 and 4.5 (a) revealed that an initial *Isp* of 400 sec achieves a lower fuel consumption and deceleration rate than an initial *Isp* value of 220 sec. To accomplish the precision landing requirements, different initial values of *Isp* are implemented in the proposed EDL maneuver for the exoatmospheric and powered descent phase. Table 4.8 – 4.10 provides an overview of the initial, entry, atmospheric conditions and rocket performance parameters that were used to generate Fig. 4.6 (a) – (d).

Table 4.8: Initial conditions, entry conditions and rocket performance parameters representing the exoatmospheric thrust phase for Fig. 4.6.

Variable	Numeric Value
h_{TA1}	140,000 m
Isp_{TA1}	400 sec
$m_{0\text{-}TA1}$	1000 kg
$t_{i\text{-}TA1}$	0.0 s
$t_{f\text{-}TA1}$	179.3098 sec
T/W_{TA1}	3
$v_{x\text{-}TA1}$	4906.2 m/s
$v_{y\text{-}TA1}$	0.0 km/s
$v_{z\text{-}TA1}$	-1097.5 m/s
ϕ_{TA1}	9.2º
θ_{TA1}	0º
$\Delta\varepsilon_{\alpha\text{-}TA1}$	-0.56
$\Delta\varepsilon_{\beta\text{-}TA1}$	0.0
$\Delta\varepsilon_{\gamma\text{-}TA1}$	0.222

Table 4.9: Initial and atmospheric conditions representing the atmospheric transit phase for Fig. 4.6.

Variable	Numeric Value
A	5.52 m^2
C_D	1.7
m_{BA}	491.1146 kg
$t_{i\text{-}BA}$	179.3098 sec
$t_{f\text{-}BA}$	832.8144 sec
ω_m	7.0882 x 10^{-5} rad/s

Table 4.10: Initial conditions and rocket performance parameters representing the powered descent and landing phase for Fig. 4.6.

Variable	Numeric Value
h_{TA2}	1,385.1466 m
Isp_{TA2}	220 sec
$m_{0\text{-}TA2}$	491.1146 kg
$t_{i\text{-}TA2}$	832.8144 sec
$t_{f\text{-}TA2}$	867.1249 sec
T/W_{TA2}	2.82

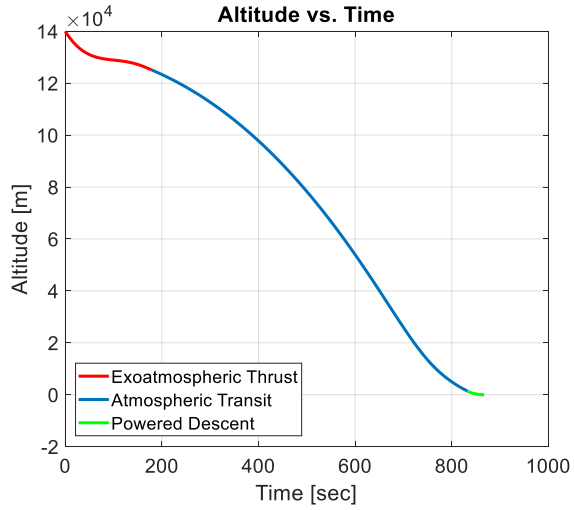

(a) Altitude vs. Time

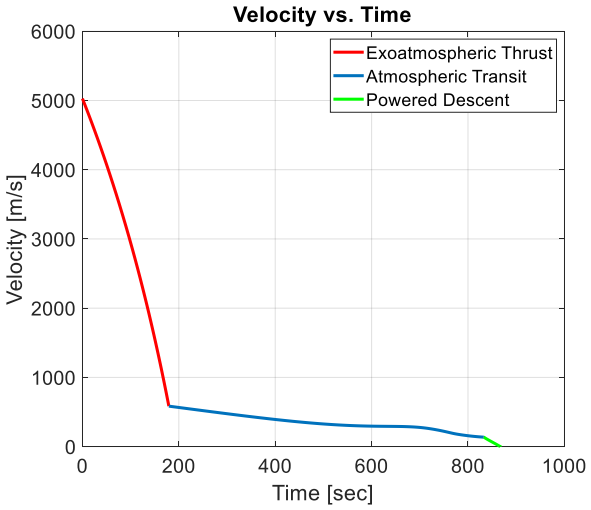

(b) Velocity vs. Time

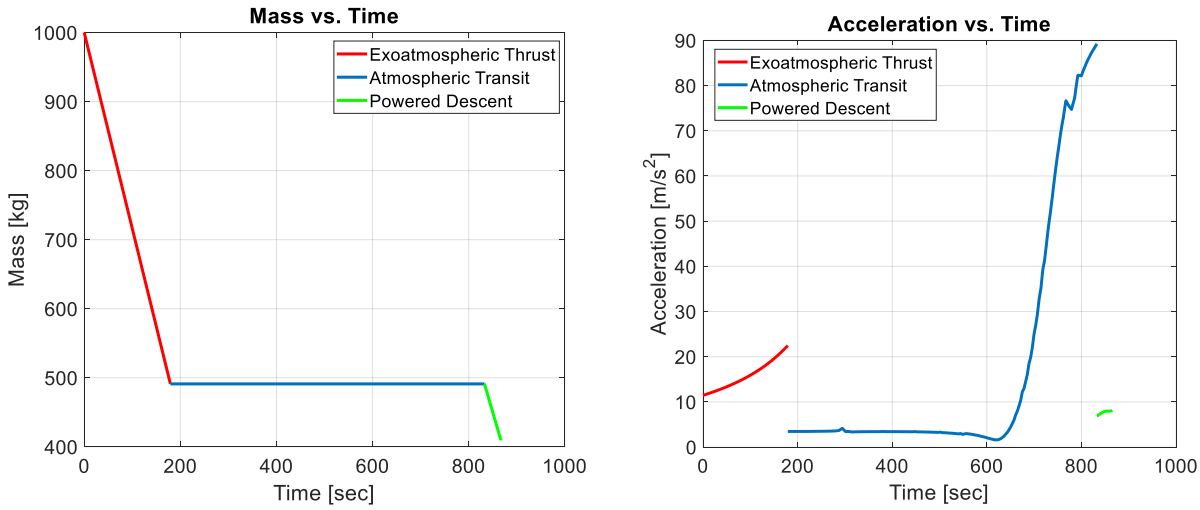

(c) Mass vs. Time (d) Acceleration vs. Time

Figure 4.6: Synthesized EDL maneuver.

The overall duration of the EDL maneuver was reduced by investigating different combinations of error term values for the exoatmospheric thrust phase. The design space considered the optimal thrust-vectoring angle of 0.8º [41], where the summation of the error term angles must be less than or equal to the desired condition. This study determined values for $\Delta\alpha$, $\Delta\beta$ and $\Delta\gamma$ through trial and error until the lander achieved a final *h* of approximately 125,000 m and v within 500 – 800 m/s as shown in Fig. 4.6 (a) and (b). A desired range for v was established since Fig. 4.4 (b) showed that a v less than 100 m/s resulted in longer duration for the lander to descend, where the blue curve begins at an initial v of 50 m/s with a duration of approximately 2,000 sec. In addition to the *h* and v requirement, another focus for the exoatmospheric thrust phase was to minimize the amount of fuel consumed. Thus, the *Isp* value was defined as 400 sec with an initial *T/W* value of 3 (see in Table 4.8) based on previous results described in subsection 4.3.

In Fig. 4.6 (b) and (d), the dramatic discontinuity at the final point of the exoatmospheric thrust and atmospheric transit phase are attributed to the set-up of the dynamical model for each phase. This includes the sudden presence of drag force acceleration, removing continuous thrusting during the atmospheric transit phase and characterizing different rocket performance parameters for the initial and final phase of the entire EDL maneuver. The exoatmospheric thrust phase specifies an initial *Isp* of 400 and *T/W* value of 3, while the powered descent and landing

phase utilized an initial *Isp* value of 220 sec with a *T/W* value of 2.82 to accomplish the primary precision landing goals.

High acceleration spikes displayed in Fig. 4.6 (d) when *t* is approximately 770 and 790 sec, is the result of using a different ordinary differential equations (ode) solver, ode45, in MATLAB for the atmospheric transit phase. Earlier stages of this work revealed complications of using the same ode solver for each phase, where moderate to high stiffness would occur for both thrust phases during the parameter selection stage. The MATLAB solver, ode15s was used for the exoatmospheric and powered descent and landing phase. Previous studies from Wiebe and Christopoulos (2010), have confirmed that acceleration spikes are expected for near degrees of freedom with relatively small masses and particularly, when change occurs from low to high stiffness traveling at high velocities [50].

The lander completes the maneuver for the atmospheric transit phase by achieving an *h* of approximately 1,385 m as shown in Figure 4.6 (a) and finally achieves an *h* of -2.4 m, v of 0.02 m/s and *m* of 410 kg upon landing. In addition to accomplishing the precision landing goals with minimal fuel consumption, Fig. 4.6 (a) – (d) demonstrated a significant decrease in duration in comparison to the trajectory envelopes generated in subsection 4.3 – 4.5. Table 4.11 provides an overview of the junction point parameters of the synthesized trajectory.

Table 4.11: Junction point parameters for the synthesized EDL maneuver.

	h (m)	*v* (º)	*p* (m)	*e*	*ω* (º)	v (m/s)	*t* (s)
Junction Point 1	1.2506 x 10^5	180.2233	3.4863 x 10^6	0.9725	108.1501	584.756	179.3098
Junction Point 2	1385.1466	180.0423	3.3923 x 10^6	0.9992	74.5158	136.7713	832.8144
Landing Site	-2.4173	180.0000	3.3895 x 10^6	1.0000	69.3863	0.0250	867.1249

4.7 Lunar Powered Descent Phase

The lunar powered descent phase adopts a significant portion of analysis from the previous trade studies described in subsections 4.1 – 4.6. Fig. 4.7 (a) – (c) are trajectory envelopes generated by varying the error term values for the thrust-vector angle. The results from subsection 4.6 confirmed that varying the error term values was the most optimal method for accomplishing the mission requirements. This study investigates five different case scenarios, where several combinations were considered by fixing 1º at specified variables. Although the

summation of error term values exceeds the optimal thrust-vectoring angle from Reference 41, this study primarily focuses on how non-zero error term values affects the overall behavior of the trajectory on the Moon. A legend is provided in each figure to distinguish the differences between the behavior of each trajectory. Table 4.12 summarizes the initial, entry conditions and rocket performance parameters representing Fig. 4.7.

Table 4.12: Initial conditions, entry conditions and rocket performance parameters representing the lunar descent phase for Fig. 4.7.

Variable	Numeric Value
h_{LD}	15,240 m
Isp_{LD}	220 sec
$m_{0\text{-}LD}$	4,000 kg
$t_{i\text{-}LD}$	0.0 s
T/W_{LD}	3
$v_{x\text{-}LD}$	1,372.23 m/s
$v_{y\text{-}LD}$	0.0 km/s
$v_{z\text{-}LD}$	-994.46 m/s
ϕ_{LD}	10º
θ_{LD}	0º

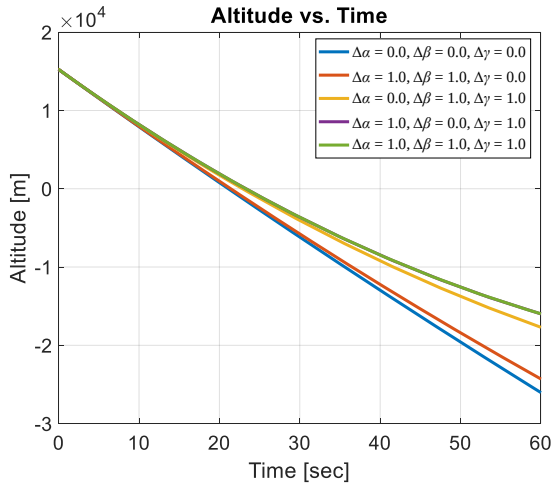

(a) Altitude vs. Time

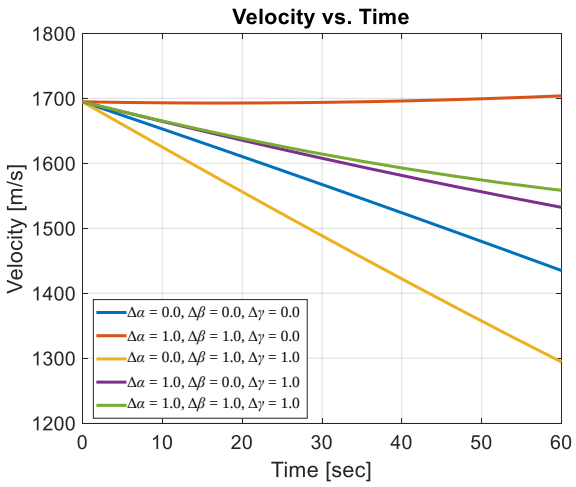

(b) Velocity vs. Time

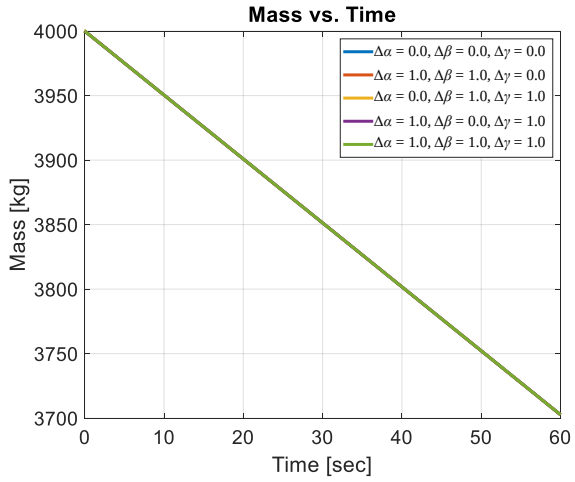

(c) Mass vs. Time

Figure 4.7: Trajectory envelopes for the lunar powered descent phase.

In Fig. 4.7 (a), the lander descends beyond the Moon's surface which is a result of specifying a time-step without any boundary conditions for *h*. The dynamical model fixed an arbitrary value of 60 sec as the final *t* of the maneuver to examine the different behaviors of the powered descent and landing trajectory. The landing *h* ranged from -2.5 - -1.5 x 10^4 m where the non-zero error term angles gradually descend beyond the surface in comparison to the blue curve (see in Fig. 4.7 (a)). In Fig. 4.7 (b), the yellow curve where $\Delta\beta$ and $\Delta\gamma$ are non-zero values, portray the lander descending quickly while Fig. 4.7 (c), there is no change in the mass for the five different cases. The following subsection will discuss a rudimentary study on the lunar ascent phase.

4.8 Lunar Ascent Phase

The lunar ascent phase begins at the surface of the Moon and achieves an *h* of 15,000 m. A similar approach from subsection 4.7 was considered for this study, however the analysis heavily focuses on the final v and whether the lander reaches the desired *h*. Table 4.13 summarizes the initial conditions and rocket performance parameters representing Fig. 4.8.

Table 4.13: Initial conditions and rocket performance parameters representing the lunar ascent phase for Fig. 4.8.

Variable	Numeric Value
Isp_{LA}	300 sec
$m_{0\text{-}LA}$	3,625.6913 kg
$t_{i\text{-}LA}$	0.0 s
$t_{f\text{-}LA}$	100.0 s
T/W_{LA}	6.4

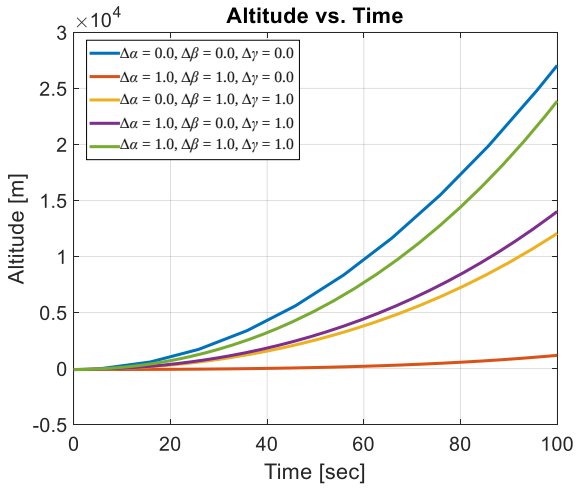

(a) Altitude vs. Time

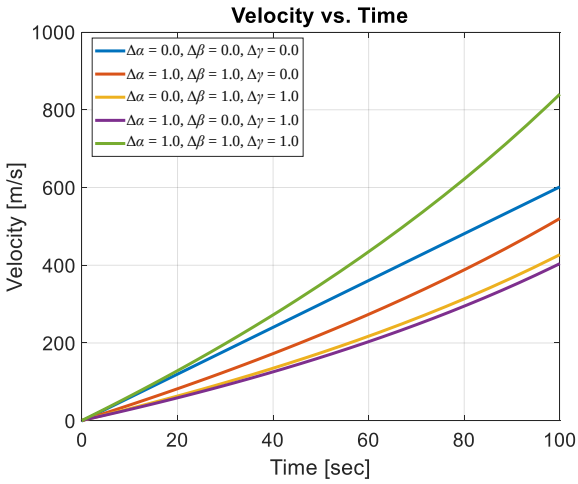

(b) Velocity vs. Time

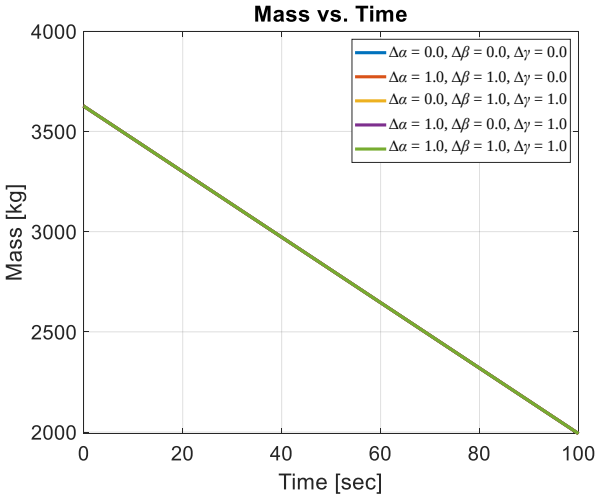

(c) Mass vs. Time

Figure 4.8: Trajectory envelopes for lunar ascent maneuver.

In Fig. 4.8 (a), the trajectory envelopes for the lunar ascent maneuver achieves an *h* range of approximately 0.1 – 2.6 x 10^4 m. The specified error term values of $\Delta\alpha$ and $\Delta\gamma$ (purple curve) achieved a desired *h* of approximately 15,000 m and v of 400 m/s as shown in Fig. 4.8 (b). However, the escape speed, which is defined as the minimum speed required for the spacecraft to be freed from the gravitational influence of a body [36], is roughly 2,376 m/s from the surface of the Moon. Based on the v profiles in Fig. 4.8 (b), the specified error term values of $\Delta\alpha$, $\Delta\beta$ and $\Delta\gamma$ (green curve) achieved a final v of approximately 820 m/s which is significantly lower than the escape velocity. This implies that an additional impulse maneuver is a potential solution for

the spacecraft to continue into orbit. Similar to Fig. 4.7 (c), there is no change in the mass (see in Fig. 4.8 (c)) where the amount of fuel consumed is roughly 1,600 kg.

CHAPTER 5
SIMULATIONS

5.1 Trajectory Envelopes

The three EDL phases were generated separately, while the final conditions upon each phase were manually connected to create the entire maneuver for both cases shown in Fig. 5.1 and 5.2. The trajectory envelopes presented in this paper utilized the proposed design space based on previous Mars missions and data collected from preliminary studies [46]. For the exoatmospheric thrust phase, the maneuver begins at an *h* of 140,000 m where the lander descends to an *h* of 125,000 m (Mars atmosphere), within a v of 500 – 800 m/s. From subsection 4.4 and 4.6, it was determined that the values outside of the 500 – 800 m/s range revealed inconsistencies with deceleration of the lander, where an increase in v and duration occurs in the later part of the maneuver. During the atmospheric transit phase, the lander attempts to achieve an *h* of 1,300 m which is the approximate *h* that was accomplished during the Curiosity Mission [6]. Finally, the primary objectives for the powered descent and landing phase consists of the lander decelerating to less than 1 m/s upon touch down within *h* range of ±100 m.

This study focuses on a comparison of two trajectory envelopes that specifies two or three non-zero initial entry v components (v_{x0}, v_{y0}, v_{z0}). The first case (A) defines the initial v_{x0} and v_{z0} as non-zero constants, while the initial v_{y0} is zero. The second case (B) defines all three initial entry v components as non-zero constants. The initial conditions that were used for both cases are as follows: $T/W = 3$; $\theta = 0^{o}$; $m_0 = 1000$ kg; $\Delta\gamma = -0.56^{o}$; $\Delta\beta = 0^{o}$; $\Delta\gamma = 0.222$; $v_{x0} = 5065$ m/s; $v_{z0} = -1300$ m/s. In addition, case B designates v_{y0} as -1000 m/s for the exoatmospheric thrust phase. The powered descent and landing phase for case A used an initial *Isp* value of 220 sec while case B was 400 sec. The initial conditions for this study was retrieved from previous results [34, 35], where feasible planar trajectories were generated in the *x* and *z* directions of the cartesian coordinate system. Table 5.1 and 5.2 summarizes a list of initial conditions that were determined through trial and error methods to fulfill the desired objectives for the exoatmospheric thrust phase and the precision landing requirements for the powered descent and landing phase.

Table 5.1: Varying initial entry ϕ values for the exoatmospheric thrust phase with an increment step size of 20 sec for initial *Isp* values.

Exoatmospheric Thrust Phase		
	Case A (v_{y0} = 0 m/s)	**Case B** (v_{y0} = -1000 m/s)
Isp (sec)	ϕ (º)	ϕ (º)
400	11	10.8
380	11	10.8
360	10.95	10.75
340	10.93	10.7
320	10.89	10.66
300	10.87	10.66
280	10.82	10.6
260	10.78	10.56
240	10.73	10.52
220	10.68	10.48

Table 5.2: Varying initial *T/W* values for the powered descent and landing phase where Case A and B utilizes an initial *Isp* of 220 and 400 sec respectively.

Powered Descent and Landing Phase	
Case A (v_{y0} = 0 m/s)	**Case B** (v_{y0} = -1000 m/s)
T/W	*T/W*
3.2	2.825
3.07	2.56
3.116	2.65
2.92	2.56
2.858	2.54
2.556	2.315
2.539	2.326
2.3	2.335
2.224	2.19
2.023	2.03

The trajectory envelopes displayed in Fig. 5.1 and 5.2 represent *h*, v, *m* of the propellant and acceleration over the duration of the entire EDL maneuver. Each figure illustrates the three EDL phases and provides a legend of summarized initial conditions that were specified for the desired trajectory of interest. In both cases, the exoatmospheric thrust phase demonstrated that an initial *Isp* of 400 sec consumes approximately 520 kg of propellant while an initial *Isp* of 220 sec is 700 kg respectively (see Figure 5.1 (c) and Figure 5.2 (c)). For the powered descent and landing phase, each case utilized a different initial *Isp* value and *T/W* value to fulfill the landing objectives. The fuel consumption is approximately double the amount in case A which used an initial *Isp* of 220 sec. However, case B displays higher spikes in acceleration where the initial *Isp*

was a value of 400 sec. Overall, utilizing an initial *Isp* of 400 sec during the exoatmospheric phase achieved an efficiency in fuel consumption while spending less time performing the entire EDL maneuver. The duration in comparison with an initial *Isp* of 220 sec is approximately 800 sec for an initial *Isp* of 400 sec versus 1,000 sec as shown in both Figures. Both cases were generated in two-dimensions, where specifying parameters for the *x* and *z* coordinate system provided favorable results from the previous studies conducted from subsection 4.1 and 4.2. The trajectory envelopes in Fig. 5.1 and 5.2 confirm that precise landing with minimal fuel consumption is achievable and will not impact the overall behavior of the EDL maneuver when v_{y0} is zero or a nonzero constant.

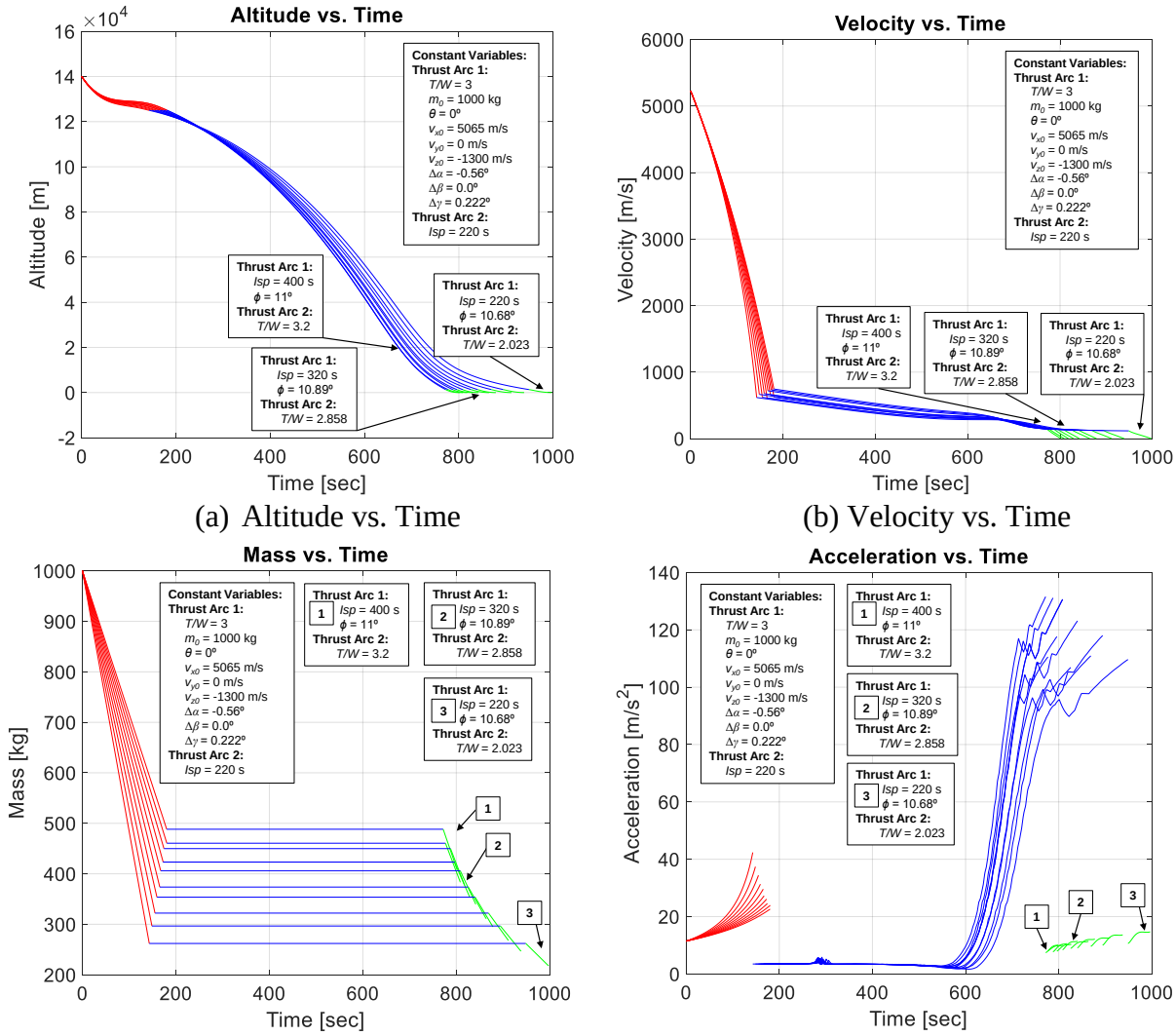

(a) Altitude vs. Time

(b) Velocity vs. Time

(c) Mass vs. Time

(d) Acceleration vs. Time

Figure 5.1: Trajectory envelopes of case A.

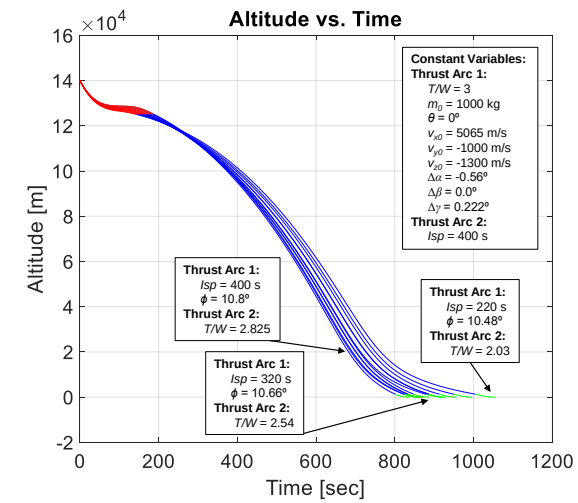

(a) Altitude vs. Time

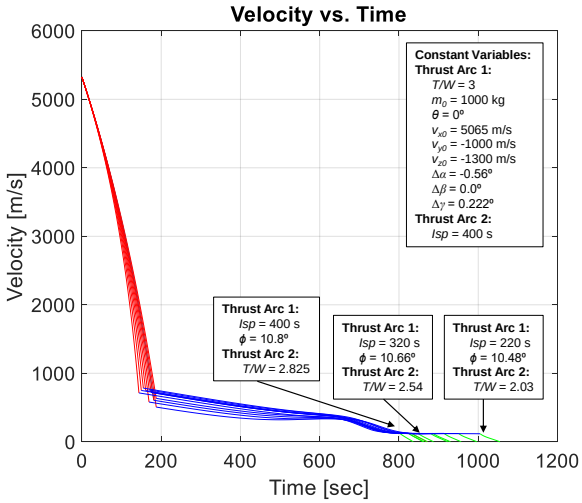

(b) Velocity vs. Time

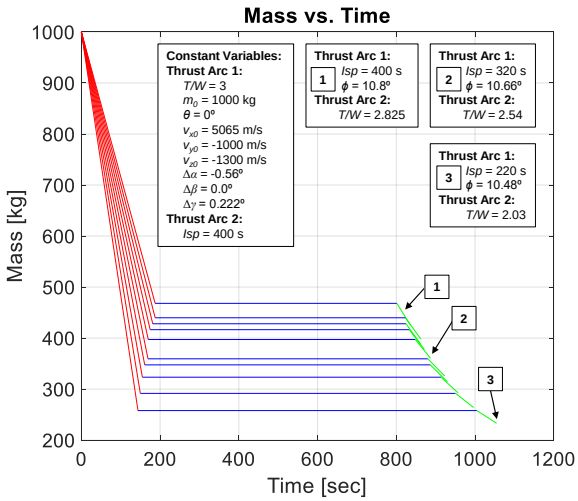

(c) Mass vs. Time

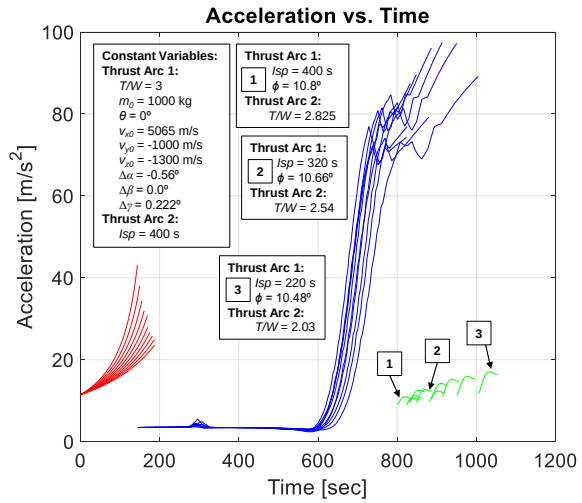

(d) Acceleration vs. Time

Figure 5.2: Trajectory envelopes of case B.

The EDL maneuver results presented in this subsection are similar to the Mars Exploration Rover and Mars Science Laboratory mission for the atmospheric transit and powered descent and landing phase [4]. This study used a numerical approach instead of a Monte Carlo analysis to allow for diverse and wide range of parameter selection and considers an additional impulse maneuver, the exoatmospheric thrust phase, where indirect entry is proposed as a solution to quickly decelerate the lander while gradually descending into Mars' atmosphere. Parachute deployment was used for previous missions at low altitudes with significantly small values of density as shown in Fig. 3.2, where majority of the sensitivity occurs during lower altitude portion of the atmospheric transit phase. To increase the overall accuracy of the

atmospheric transit phase, future studies will incorporate a parachute model as the next complexity into the current dynamical model.

5.2 Manifold of landing points: Measure of accuracy of landing

A summary of landing points was collected and plotted along a set of three two-dimensional axes: x versus y, y versus z and x versus z. The designated landing site for both cases was determined by averaging the landing points. The junction point parameters were determined for the trajectory that was near the designated landing site as described in Table 5.3 and 5.4 and illustrated in Fig. 5.3 and 5.4. The lander that was the closest to the designated landing site was case B along the x and z axis shown in Fig. 5.4 (c).

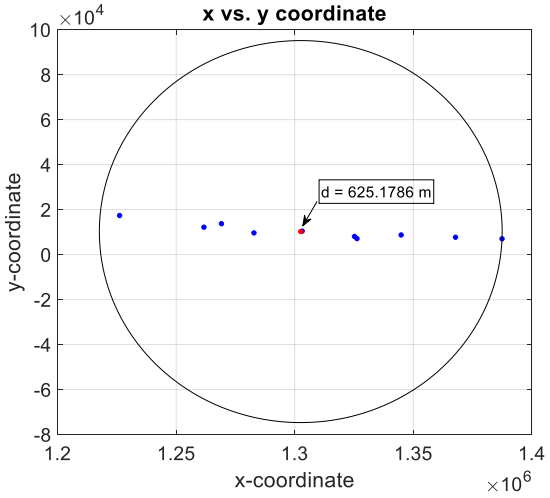

(a) x vs. y

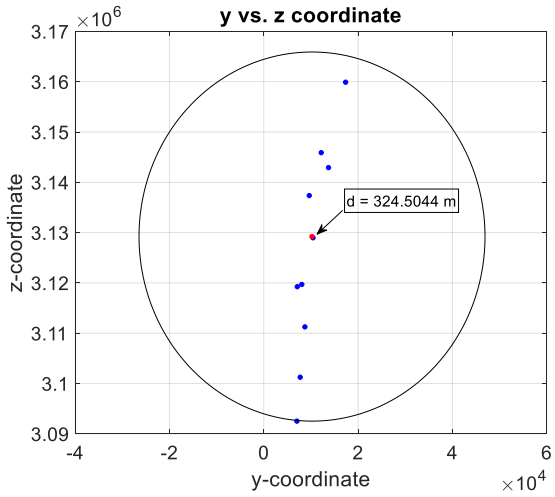

(b) y vs. z

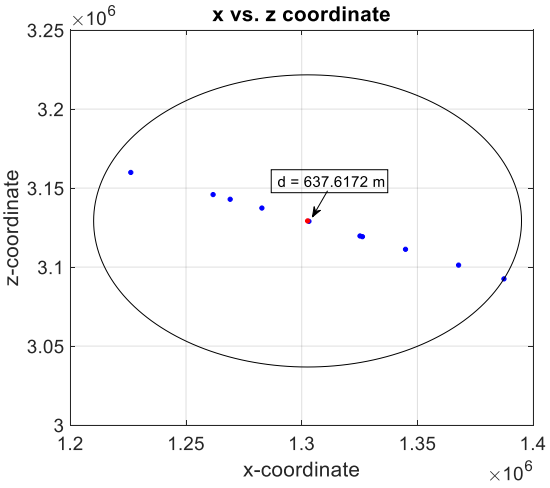

(c) x vs. z

Figure 5.3: Landing ellipse for case A.

Table 5.3: Junction Point Parameters for case A with a designated landing site of ϕ = 22.6 and θ = 0.45.

	h (m)	V (º)	p (m)	e	ω (º)	v (m/s)	t (s)
Junction Point 1	1.2504 x 10^5	180.2259	3.5200 x 10^6	0.9629	109.4883	676.1847	159.4149
Junction Point 2	1296.7075	180.0326	3.3928 x 10^6	0.9990	74.9102	128.1307	840.3616
Landing Site	-0.3252	180.0000	3.3895 x 10^6	1.0000	67.3898	0.0015	878.4491

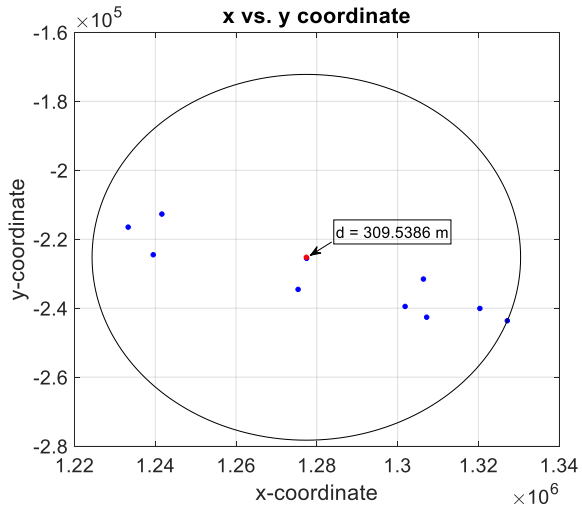

(a) x vs. y

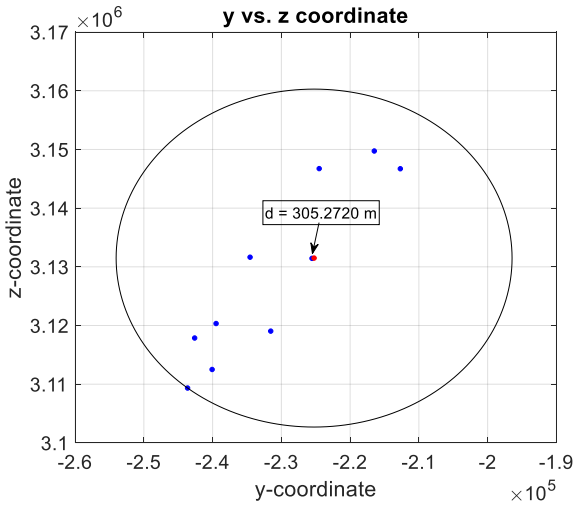

(b) y vs. z

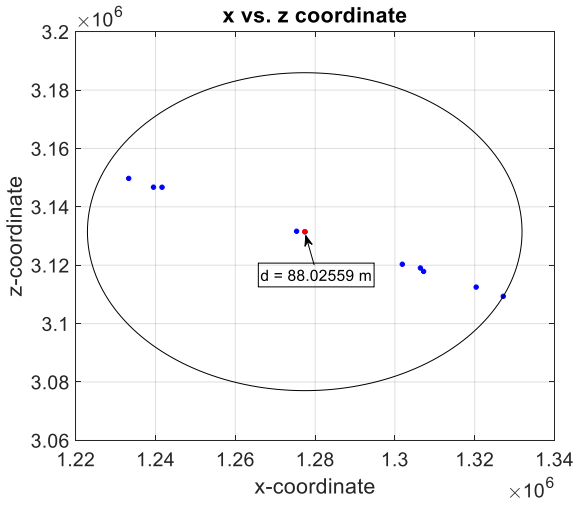

(c) x vs. z

Figure 5.4: Landing ellipse for case B.

Table 5.4: Junction Point Parameters for case B with a designated landing site of ϕ = 22.5 and θ = -10

	h (m)	v (º)	p (m)	e	ω (º)	v (m/s)	t (s)
Junction Point 1	1.2503 x 10^5	180.2394	3.4934 x 10^6	0.9704	109.3439	605.9245	181.3631
Junction Point 2	1227.5336	180.0322	3.3923 x 10^6	0.9992	72.1381	123.4288	824.7268
Landing Site	0.3891	180.0000	3.3895 x 10^6	1.0000	67.7646	0.0015	861.3796

5.3 Lunar Powered Descent and Ascent Phase

The proposed research focused on providing a solution that will achieve the precision landing requirements which is presented in Fig 5.5 and 5.6 (a) – (c). Table 5.5 and 5.6 summarizes the conditions used to generate the plots in Fig. 5.5.

Table 5.5: Initial conditions, entry conditions and rocket performance parameters representing the lunar descent phase for Fig. 5.5

Variable	**Numeric Value**
h_{LD}	15,240 m
Isp_{LD}	220 sec
$m_{0\text{-}LD}$	4,000 kg
$t_{i\text{-}LD}$	0.0 s
T/W_{LD}	3
$v_{x\text{-}LD}$	1,372.23 m/s
$v_{y\text{-}LD}$	0.0 km/s
$v_{z\text{-}LD}$	-994.46 m/s
ϕ_{LD}	10º
θ_{LD}	0º

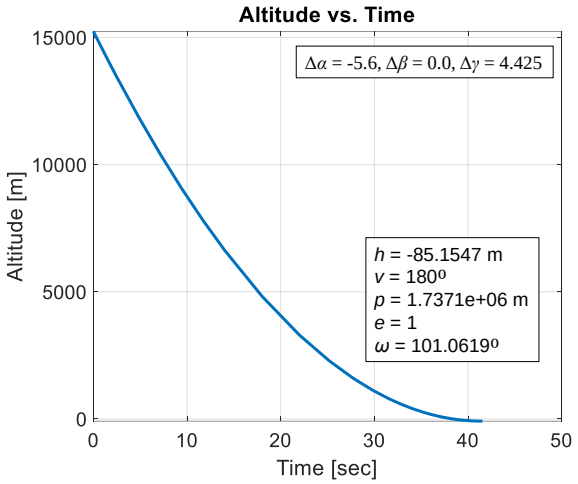

(a) Altitude vs. Time

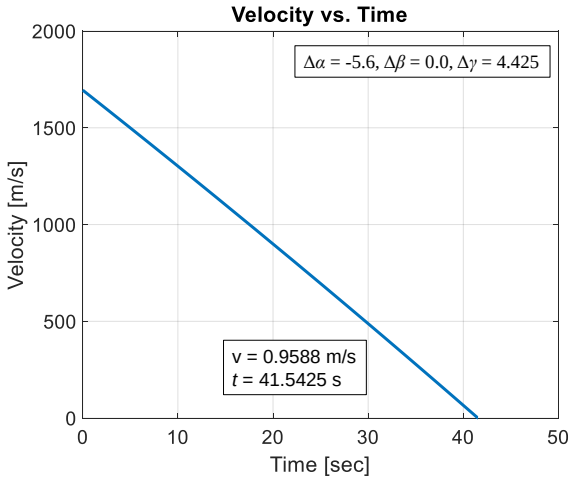

(b) Velocity vs. Time

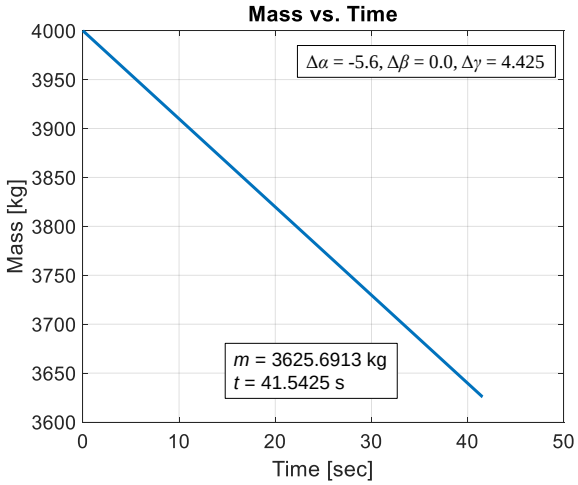

(c) Mass vs. Time

Figure 5.5: Lunar powered descent trajectory.

Table 5.6: Initial conditions, entry conditions and rocket performance parameters representing the lunar ascent phase for Fig. 5.6

Variable	Numeric Value
Isp_{LA}	300 sec
$m_{0\text{-}LA}$	3,625.6913 kg
$t_{i\text{-}LA}$	0.0 s
$t_{f\text{-}LA}$	100.0 s
T/W_{LA}	6.4

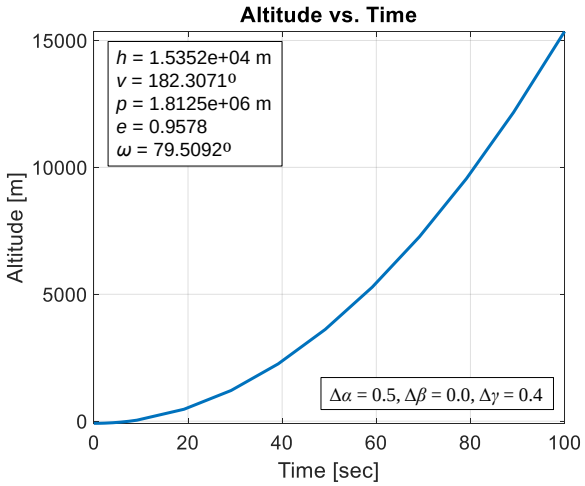

(a) Altitude vs. Time

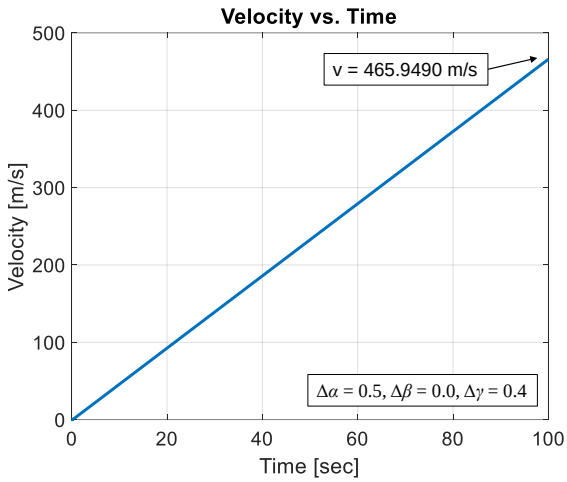

(b) Velocity vs. Time

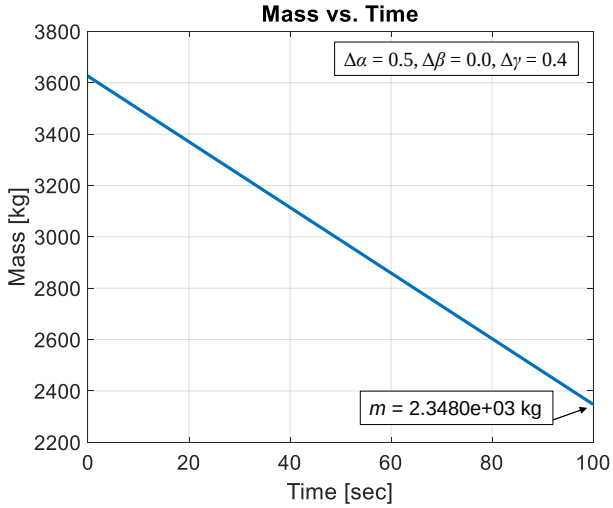

(c) Mass vs. Time

Figure 5.6: Lunar ascent trajectory.

CHAPTER 6
CONCLUDING REMARKS

The envelopes that were generated for each phase of the proposed EDL maneuver revealed that it is possible to design and customize a trajectory with a specific set of initial entry conditions. A design and construction of synthesized trajectory envelopes which achieved the primary precision landing requirements are presented. This study shown that the rocket performance parameters can be different for both the exoatmospheric transit and powered descent phase as long as the precision landing requirements are met. The entry velocity components in the *x* and *z* direction of the cartesian coordinate system were arbitrary values that were finalized through trial and error during the initial stages of this work along with other crucial parameters that were constantly adjusted. The entry-spherical coordinate system, rocket performance parameters and drag model were refined to ensure that a synthesized EDL maneuver was feasible. The entry conditions, particularly, the initial velocity components, thrust angles and spherical coordinates had a significant impact to the overall profile of the trajectory. The three-dimensional model provided an acceptable landing accuracy, where spherical coordinates are designated based on the creation of the trajectory envelope. For the lunar descent and ascent maneuver, the basic precision landing requirements were achieved and the ascent *h* reached 15,000 by varying the error term components for $\Delta\alpha$ and $\Delta\gamma$.

Future work will involve further extension of the trajectory envelopes that considers broader numerical ranges for the spherical coordinate θ, the thrust angles, thrust parameters along with guidance commands. Continuation of this work will also include construction and design of additional trajectories superimposed with each phase connected to form the entire EDL maneuver for lunar missions. These trajectories will be combined to formulate an envelope, providing multiple solutions to achieving precise landing at various initial and final conditions. Eventually, the proposed envelope will be further refined by modifying trajectories to improve the landing accuracy of the EDL maneuver. The current model requires further refinement where other cases for entry conditions can be considered to improve and increase the overall accuracy and efficiency of the lander's fuel expenditures. Desired trajectories within the proposed envelopes will eventually be extracted into a customized envelope that will incorporate added complexities to fulfill the mission design tasks for the future landing missions on the Moon to the

southern poles. Optimization methods for lunar descent and ascent maneuvers will be considered for further investigation to provide longer duration to perform the maneuver.

BIBLIOGRAPHY

[1] A. E. Johnson, A. R. Klumpp, J. B. Collier and A. A. Wolf, "Lidar-based Hazard Avoidance for Safe Landing on Mars," *AIAA Journal*, Vol. 25, No. 6, 2002, pp. 1091, 1099.

[2] T. P. Rivellini, *Frontiers of Engineering: Reports on Leading-Edge Engineering from the 2004 NAE Symposium on Frontiers of Engineering*, National Academy of Sciences, Washington, D.C., 2005, pp. 23, 31.

[3] R. D. Braun and R. M. Manning, "Mars Exploration Entry, Descent and Landing Challenges," *AIAA Journal*, Vol. 44, No. 2, 2007, pp. 310, 323.

[4] "NASA Technology Roadmaps TA 9: Entry, Descent and Landing Systems." National Aeronautics and Space Administration. May 2015 Draft. Retrieved on August 21, 2019. https://www.nasa.gov/sites/default/files/atoms/files/2015_nasa_technology_roadmaps_ta_9_entry_descent_landing.pdf.

[5] National Research Council, *NASA Space Technology Roadmaps and Priorities: Restoring NASA's Technological Edge and Paving the Way for a New Era in Space*. Washington, DC: The National Academies Press. 2012, pp. 256. https://doi.org/10.17226/13354.

[6] Z. Yu, P. Cui, and J. L. Crassidis, "Design and optimization of navigation and guidance techniques for Mars pinpoint landing: Review and prospect," *Progress in Aerospace Sciences*, Elsevier, Vol. 94, 2017, pp. 82 – 94.

[7] P. N. Desai and P. C. Knocke, "Mars Exploration Entry, Descent and Landing Trajectory Analysis," *Journal of the Astronautical Sciences*, Vol. 55, No. 3, 2007, pp. 311 – 323.

[8] B. K. Muirhead and A. Karp, "Mars Sample Return Lander Mission Concepts," *2019 IEEE Aerospace Conference*, Big Sky, Montana, 2 – 9 March 2019.

[9] A. Sengupta, A. Steltzner, A. Witkowski, J. Rowan and J. Cruz. "Overview of the Mars Science Laboratory Parachute Decelerator Subsystem." IEEE Aerospace Conference, Big Sky, Montana, March 3 – 10, 2007. pp.1 – 9.

[10] K. J. Murphy, et al. "Orion Crew Module Aerodynamic Testing," *29th AIAA Applied Aerodynamics Conference*, AIAA Paper 2011-3502, June 27 – 30, 2011. Honolulu, HI.

[11] "Planetary Mission Entry Vehicles Quick Reference Guide" NASA Ames Research Center. Version 3. NASA/SP-2006-3401.

[12] D. Beaty, M. Grady, L. Mayand and B. Gardini, "Preliminary Planning for an International Mars Sample Return," International Mars Architecture for the Return of Samples (iMARS), 1 June 2008. pp. 1 – 60.

[13] C.R. Neal, et al. “Developing Sample Return Technology using the Earth’s Moon as a Testing Ground.” Inner Planets Panel, NRC Decadal Survey. 2013.

[14] A. H. Treiman, et al. “Sample Return from the Earth’s Moon,” Curation and Analysis Planning Team for Extraterrestrial Materials (CAPTEM). White Paper Submitted to 2009 NRC Planetary Decadal Survey. Rev. Sept. 2009.

[15] D. Williams, “Ice on the Moon A Summary of Clementine and Lunar Prospector Results,” NASA Goddard Space Flight Center. December 2012. Retrieved on Oct. 4, 2018. https://nssdc.gsfc.nasa.gov/planetary/ice/ice_moon.html.

[16] C.M. Pieters, et al. “Character and Spatial Distribution of OH/H_2O on the Surface of the Moon Seen by M^3 on Chandrayaan-1,” Sciencexpress. 10.1126/science.1178658. 24 September 2009.

[17] A., Colaprete, et al. “Detection of Water in the LCROSS Ejecta Plume,” Science. Vol. 330, Issue 6003, pp. 463 – 468. 10.1126/science.1186986. 22 Oct. 2010.

[18] L., Shuai, et al. “Direct Evidence of Surface Exposed Water Ice in the Lunar Polar Regions,” Proceedings of the National Academy of Sciences, doi: 10.1073/pnas.1802345115. 2018.

[19] B. Dunbar and T. Greicius, “Landing Accuracy on Mars: A Historical Perspective,” NASA. August 10, 2012. https://www.nasa.gov/mission_pages/msl/multimedia/pia16039.html. Retrieved on August 21, 2019.

[20] P. C. Knocke, G. G. Wawrzyniak, B. M. Kennedy, P. N. Desai, T. J. Parker, T. C. Golombek, M. P. Duxbury and D. M. Kass, “Mars Exploration Rovers Landing Dispersion Analysis,” *AIAA/AAS Astrodynamics Specialist Conference and Exhibit*, Providence, Rhode Island, 16 – 19 August, 2004. doi:10.2514/6.2004-5093.

[21] P. D. Burkhart and J. Casoliva, “MSL DSENDS EDL analysis and operations,” *23rd International Symposium on Space Flight Dynamics (ISSFD),* Pasadena, California, October 29 – November 2, 2012.

[22] “InSight’s Landing Site: Elysium Planitia,” MARS InSight Mission. Retrieved on August 21, 2019. https://mars.nasa.gov/insight/timeline/prelaunch/landing-site-selection/.

[23] M. Lavagna, C. Parigini and R. Armellin, “Pso Algorithm For Planetary Atmosphere Entry Vehicles Multidisciplinary Guidance Design,” *AIAA/AAS Astrodynamics Specialist Conference and Exhibit,* Keystone, Colorado, 21 – 24 August 2006.

[24] M. Grant, and G. Mendeck, (2007) “Mars Science Laboratory Entry Optimization Using Particle Swarm Methodology,” *AIAA Atmospheric Flight Mechanics Conference and Exhibit*, Hilton Head, South Carolina, 20 – 23 August 2007.

[25] R. Arora, “Reentry Trajectory Optimization: Evolutionary Approach,” *9th AIAA/ISSMO Symposium on Multidisciplinary Analysis and Optimization,* Atlanta, Georgia, 4 – 6 September 2002.

[26] G. Chen, Z. Wan, M. Xu, and S. Chen, "Genetic Algorithm Optimization of RLV Reentry Trajectory," *AIAA/CIRA 13th International Space Planes and Hypersonics Systems and Technologies Conference*, Capua, Italy, 16 – 20 May 2005.

[27] N. Yokoyama, and S. Suzuki, "Modified Genetic Algorithm for Constrained Trajectory Optimization," *Journal of Guidance, Control, and Dynamics*, Vol. 28, No. 1, January 2005.

[28] L. Soler, A. Khatib and K. D. Mease, "Mars Entry Trajectory Planning for Higher Elevation Landing," *AAS/AIAA Space Flight Mechanics Meeting*, Kaua'i, Hawai'i, February 2013.

[29] G. Duan, M. R. Navarro, and K. D. Mease, "Trajectory Tracking and Online Replanning for Mars Entry," *AIAA/AAS Astrodynamics Specialist Conference,* Long Beach, California, 13 – 16 September 2016.

[30] M. Onishi. "Analysis of Landing Trajectory using Backward Propagation," *Hawaii Space Grant Consortium (HSGC) Symposium*, Honolulu, Hawaii, 23 November, 2013.

[31] M. Onishi. "Analysis of Landing Trajectory using Forward Propagation," *Hawaii Space Grant Consortium (HSGC) Symposium*, Honolulu, Hawaii, 26 April, 2014.

[32] D. M. Azimov, *Extremal Analytical Solutions for Space Trajectories*. Butterworth-Heinemann, Oxford, 2017, 330 p.

[33] D.F. Lawden. "Optimal Trajectories for Space Navigation," Butterworths, London. 1963. pp. 55-59.

[34] M. M. Onishi and D. M. Azimov, "Design and Synthesis of Entry, Powered Descent and Landing Maneuver Trajectories using Motion Envelopes," AAS/AIAA Astrodynamics Specialist Conference, Portland, Maine, 11 – 15 August 2019, pp. 1 – 15.

[35] M. M. Onishi and D. M. Azimov, "Design and Analysis of Entry, Powered Descent Trajectory Envelopes and Manifold of Landing Points," *International Journal of Space Science and Engineering*, Submitted for Review: October 31, 2019.

[36] H. D. Curtis, *Orbital Mechanics for Engineering Students*, 3rd ed., Elsevier Ltd., Oxford, UK, 2014, pp. 658.

[37] D. M. Azimov and R.H. Bishop, "Integrated Targeting and Guidance for Powered Planetary Descent," *The Journal of the Astronautical Sciences*, Vol. 65, Issue 2, 2018, pp. 229-259.

[38] D. A. Vallado, *Fundamentals of Astrodynamics and Applications*. 1997. McGraw-Hill. P. 922.

[39] T. L. Yang, "A Targeting Scheme for Fuel Optimal Rocket Trajectories with Applications to the LM Descent and Braking Phase, Technical Memorandum TM – 71-2014-1," Bellcomm. January 22, 1971. pp. 25.

[40] R. R. Sostaric and J. R. Rea, "Powered Descent Guidance Methods for the Moon and Mars," *AIAA Guidance, Navigation and Control Conference and Exhibit.* 15 – 18 August, 2005. San Francisco, California. AIAA 2005-6287, pp. 1-20.

[41] G. B. Gilyard and A. Bolonkin, “Optimal Pitch Thrust-Vector Angle and Benefits for all Flight Regimes.” NASA Technical Reports Server (NTRS), NASA/TM-2000-209021, March, 2000, pp. 9.

[42] C. D. Karlgaard, P. Kutty, M. Schoenenberger, J. Shidner and M. Munk, “Mars Entry Atmospheric Data System Trajectory Reconstruction Algorithms and Flight Results,” *Journal of Spacecraft and Rockets,* Vol. 51, No. 4, 2014.

[43] C. Holstein-Rathlou, A. Maue and P. Withers, “Atmospheric studies from the Mars Sciences Laboratory Entry, Descent and Landing atmospheric structure reconstruction,” *Planetary and Space Science,* 2016, pp. 15-23.

[44] D. E. Smith, et al. “Mars Orbiter Laser Altimeter: Experiment summary after the first year of global mapping of Mars.” *Journal of Geophysical Research*, Vol. 106, No. E10, 25 October 2001, pp. 23,696.

[45] S. C. C. Wu, “Planetary Elevation Reference Systems: Gravity or Tri-Axiality,” *Lunar and Planetary Science XV*, March 1984, pp. 943.

[46] M. Onishi and D. M. Azimov, “Design and Computation of Trajectory Envelopes for Powered Descent and Precision Landing,” Poster session presented at *AIAA Space Forum*, Long Beach, California, September, 2016.

[47] Apollo 12 Mission Report, Trajectory Reconstruction and Post-flight Analysis, Vol.1, NASA-TM-X-70272, Houston, TX, 1970.

[48] V. Y. Rygalov, J. K. Greene and J. M. Jurist, “Supersonic Survival Envelope Analysis for High Altitude Free Fall,” *44th International Conference on Environmental Systems,* Tucson, Arizona, 13-17 July 2014, pp. 3-4.

[49] D. A. Spencer, R. C. Blanchard, R. D. Braun, P. H. Kallemeyn and S. W. Thurman, “Mars Pathfinder Entry, Descent, and Landing Reconstruction,” *Journal of Spacecraft and Rockets*, Vol. 36, No. 3, May – June 1999, pp. 357 – 366.

[50] L. Wiebe and C. Christopoulos, “Characterizing acceleration spikes due to stiffness changes in nonlinear systems,” *International Association for Earthquake Engineering,* Vol. 39, Iss. 14, November 2010, pp. 1653.